AFRL-AFOSR-VA-TR-2019-0132

High Fidelity Measurements and Modeling of Combustion Instabilities

Ann Karagozian
UNIVERSITY OF CALIFORNIA LOS ANGELES
11000 KINROSS AVE STE 102
LOS ANGELES, CA 90095-0001

05/06/2019
Final Report

Air Force Research Laboratory
AF Office Of Scientific Research (AFOSR)/RTA1

Arlington, Virginia 22203
Air Force Materiel Command

REPORT DOCUMENTATION PAGE

Form Approved
OMB No. 0704-0188

1. REPORT DATE *(DD-MM-YYYY)*	2. REPORT TYPE	3. DATES COVERED *(From - To)*
06-05-2019	Final Performance	01 Aug 2015 to 31 Jan 2019

4. TITLE AND SUBTITLE
High Fidelity Measurements and Modeling of Combustion Instabilities

5a. CONTRACT NUMBER

5b. GRANT NUMBER
FA9550-15-1-0339

5c. PROGRAM ELEMENT NUMBER
61102F

6. AUTHOR(S)
Ann Karagozian

5d. PROJECT NUMBER

5e. TASK NUMBER

5f. WORK UNIT NUMBER

7. PERFORMING ORGANIZATION NAME(S) AND ADDRESS(ES)
UNIVERSITY OF CALIFORNIA LOS ANGELES
11000 KINROSS AVE STE 102
LOS ANGELES, CA 90095-0001 US

8. PERFORMING ORGANIZATION REPORT NUMBER

9. SPONSORING/MONITORING AGENCY NAME(S) AND ADDRESS(ES)
AF Office of Scientific Research
875 N. Randolph St. Room 3112
Arlington, VA 22203

10. SPONSOR/MONITOR'S ACRONYM(S)
AFRL/AFOSR RTA1

11. SPONSOR/MONITOR'S REPORT NUMBER(S)
AFRL-AFOSR-VA-TR-2019-0132

12. DISTRIBUTION/AVAILABILITY STATEMENT
A DISTRIBUTION UNLIMITED: PB Public Release

13. SUPPLEMENTARY NOTES

14. ABSTRACT
Acoustically coupled combustion instabilities can result in large scale, potentially catastrophic pressure oscillations in a range of propulsion systems, including both liquid rocket engines (LREs) and gas turbine engines. Such combustion instabilities are characterized by self-sustaining, generally spontaneously excited, large amplitude oscillations associated with natural acoustic modes established within a combustion chamber. New methods of analysis, measurement, prediction and design/development are required to make progress toward a detailed understanding of the interactions among hydrodynamics, acoustics, turbulent mixing, and chemical kinetics that control whether a combustor will be stable or unstable. Our team has undertaken a collaborative research project in which researchers at both Purdue and UCLA pursue the study of reactive flowfields that can shed light on greater understanding of these instabilities and the ability to control them in practical propulsion systems. Research at UCLA during the funding period has involved fundamental experimental studies on acoustically-coupled, condensed phase combustion processes, with a major focus on exploration of: (1) newly-discovered periodic partial flame extinction as a coupling mode for acoustically-driven non-premixed combustion; (2) the effects of nanoparticulate additives (both energetic and inert) on liquid fuel droplet combustion in quiescent surroundings, including model comparisons; (3) the effects of nanoparticulates on fuel droplet combustion in the presence of chamber-based acoustic perturbations; (4) periodic partial extinction and full extinction strain rates for nanofuels; and (5) initiation of alternative combustion configurations for further studies, especially in the gas phase. The research at Purdue has encompassed concurrent high-fidelity simulations and experimental tests of a model combustor

15. SUBJECT TERMS
high pressure combustion instability, dynamics control with nanoenergetics

16. SECURITY CLASSIFICATION OF:			17. LIMITATION OF ABSTRACT	18. NUMBER OF PAGES	19a. NAME OF RESPONSIBLE PERSON
a. REPORT	b. ABSTRACT	c. THIS PAGE			BIRKAN, MITAT
Unclassified	Unclassified	Unclassified	UU		19b. TELEPHONE NUMBER *(Include area code)* 703-696-7234

Standard Form 298 (Rev. 8/98)
Prescribed by ANSI Std. Z39.18

Final Report:

AFOSR Award No. FA9550-15-1-0339

High Fidelity Measurements and Modeling of Combustion Instabilities

A. R. Karagozian, O. I. Smith, H. S. Sim, J. Bennewitz, A. Vargas and M. Plascencia Quiroz
University of California, Los Angeles

W. E. Anderson, R. Lucht, S. Sardeshmukh, T. Fuller, and A. Pons
Purdue University

AFOSR Space Propulsion and Power Program
Dr. Mitat Birkan, AFOSR/RTE, Program Manager

August 1, 2015 – January 31, 2019

Overview

Acoustically coupled combustion instabilities can result in large scale, potentially catastrophic pressure oscillations in a range of propulsion systems, including both liquid rocket engines (LREs) and gas turbine engines. Such combustion instabilities are characterized by self-sustaining, generally spontaneously excited, large amplitude oscillations associated with natural acoustic modes established within a combustion chamber. New methods of analysis, measurement, prediction and design/development are required to make progress toward a detailed understanding of the interactions among hydrodynamics, acoustics, turbulent mixing, and chemical kinetics that control whether a combustor will be stable or unstable. Our team has undertaken a collaborative research project in which researchers at both Purdue and UCLA pursue the study of reactive flowfields that can shed light on greater understanding of these instabilities and the ability to control them in practical propulsion systems. Research at UCLA during the funding period has involved fundamental experimental studies on acoustically-coupled, condensed phase combustion processes, with a major focus on exploration of: (1) newly-discovered periodic partial flame extinction as a coupling mode for acoustically-driven non-premixed combustion; (2) the effects of nanoparticulate additives (both energetic and inert) on liquid fuel droplet combustion in quiescent surroundings, including model comparisons; (3) the effects of nanoparticulates on fuel droplet combustion in the presence of chamber-based acoustic perturbations; (4) periodic partial extinction and full extinction strain rates for nanofuels; and (5) initiation of alternative combustion configurations for further studies, especially in the gas phase. The research at Purdue has encompassed concurrent high-fidelity simulations and experimental tests of a model combustor that exhibits self-excited instabilities that are dependent on flow and geometric parameters. Experimental observations are used to motivate a detailed study of results from validated simulations for further fundamental understanding, with a focus on a single element shear coaxial injector with a propellant combination of subcritical gaseous methane and warm oxygen. The Purdue experimental design and operating conditions are well-controlled so that they can be accurately and precisely represented in concurrent simulations.

Final Report: UCLA Research Activities on Combustion Instabilities in Liquid Nanofuels
AFOSR Award FA 9550-15-1-0339, 8/1/2015-1/31/2019

A. R. Karagozian[a], O. I. Smith[b], H. S. Sim[c], J. Bennewitz[d], A. Vargas[e], and M. Plascencia Quiroz[e]

Research at UCLA during the past several years, under support from AFOSR, has primarily involved fundamental experimental studies on acoustically-coupled fuel droplet combustion processes, with a major focus on exploration of the effects of nanoparticulate additives (both energetic and inert) on alternative liquid fuels during combustion, on the effects of nanoparticulates on droplet combustion in the presence of chamber-based acoustic perturbations, and on periodic partial extinction and full extinction strain rates for neat fuels and nanofuels. These studies employ a closed, atmospheric pressure acoustic waveguide in which standing acoustic waves may be created for a range of frequencies and amplitudes; because of the nature of flame perturbations via local flame straining, focus has been placed in these studies on combustion near a pressure node (PN) or velocity antinode (VAN). In these experiments, burning fuel droplets may be either suspended from a fiber (Case I) or fine capillary (Case II), or continuously "fed" fuel via a fine capillary (Case III), the latter being required for acoustically-coupled droplet combustion experiments and phase-locked imaging. A schematic for the experiment is shown in **Figure 1(a)**, with alternative droplet suspension methods shown in **Figure 1(b)**. Details on its operation, whereby burning droplets may be situated at various locations relative to the standing acoustic waves, are available in Sevilla, et al.[1] and in a more recent paper by Bennewitz, et al.[2] The flexibly designed facility here involves the ability to move the speakers bounding the waveguide so that the fuel droplet (or other reactive structure) can be studied at positions relative to the PN/VAN, of importance in practical systems.

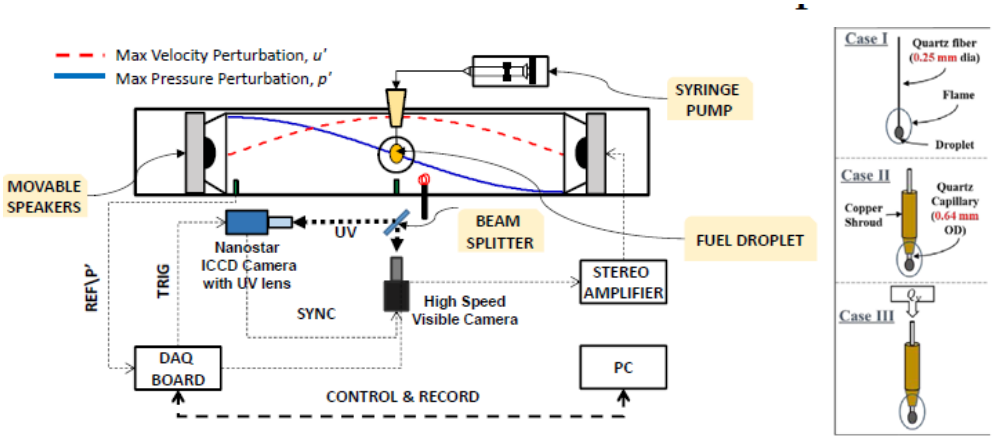

Figure 1. (a) Acoustically-coupled combustion test facility at UCLA, consisting of the acoustic waveguide, droplet feed system, measurement diagnostics (for simultaneous OH* chemiluminescence and visible imaging) and data acquisition system. Sample waveforms for the acoustic pressure and velocity are depicted for the droplet located at the pressure node (PN). (b) Three different droplet delivery systems; only Case III has continuous fuel delivery via the syringe pump.

[a] Professor, UCLA Department of Mechanical and Aerospace Engineering
[b] Professor Emeritus, UCLA Department of Mechanical and Aerospace Engineering
[c] Former UCLA Postdoctoral Scholar; currently Postdoctoral Scholar, Sandia National Laboratory Combustion Research Facility (Livermore, CA)
[d] Former UCLA Postdoctoral Scholar; currently Research Scientist, Air Force Research Laboratory, AFRL/RQRC
[e] Graduate student, UCLA Department of Mechanical and Aerospace Engineering

It should be noted that in the droplet combustion experiments, the value of the burning rate constant K was calculated on the basis of the experimental fuel delivery method. For the "non-fed" cases (I and II), the continuity equation yields K based on the "d-squared" law[3]:

$$K_{non-fed} = -\frac{d(d^2)}{dt} = -2d\dot{d} \qquad (1)$$

For "fed" droplets with continuous fuel delivery (case III), continuity accounts for this fuel delivery at volume flow rate, Q_v:

$$K_{fed} = \frac{4Q_v}{\pi d} - 2d\dot{d} \qquad (2)$$

In Eqn. (1), *K* values were extracted as the linear slope of measured d^2 vs. time plots *via* least squares linear regression, using the middle 80% of the data range, excluding the transient regimes at the beginning and end of the combustion process. For the fed droplet (eqn. (2)), the rate of change in the diameter of the droplet ($\dot{d}$) was calculated using moving average smoothing. The average initial droplet diameter measured from the high speed camera for non-fed, fiber-supported droplets was 1.291 mm. For fed droplets, the average diameter during quasi-steady state combustion was 1.889 mm; the droplet diameter was larger than for fiber-suspended non-fed droplets because of the larger quartz capillary size. The measured initial and average droplet diameters were found to be unchanged with different particle loading concentrations, particle type, and droplet imaging techniques.

Periodic Partial Extinction Exploration

Prior experimental studies by our group[1,4] have focused on neat fuel droplet combustion characteristics for alternative liquid fuels during exposure to standing acoustic waves. In response to such acoustic excitation, the flame surrounding the droplet is observed to be deflected, on average, with an orientation depending on the droplet's relative position with respect to the PN, qualitatively consistent with the sign of a theoretical bulk acoustic acceleration or acoustic radiation force, analogous to a buoyancy force[5]. Phase-locked OH* chemiluminescence imaging is used to quantify temporal, periodic oscillations in flame standoff distance as well as chemiluminescent intensity, which, coupled to local measurements of the oscillatory pressure perturbations, enables the well-known Rayleigh index *G(x)* to be quantified at various locations x within the waveguide:

$$G(x) = \frac{1}{T}\int_T p'(x,t)q'(x,t)dt \qquad (3)$$

Here a positive *G* value denotes in-phase fluctuations of pressure and heat release and hence instability, while out-of-phase *p'* and *q'* lead to a negative *G* value and presumably stable combustion, consistent with the classical Rayleigh criterion[6]. For low and moderate amplitudes of excitation, the OH* chemiluminescence intensity *I'* always increases as the flame approaches the droplet and decreases as it periodically withdraws from the droplet. This causes *I'* and p' to oscillate in phase, thus creating a positive Rayleigh Index G(x). The magnitude of the Rayleigh index is dependent on fuel, and tends to be larger for lower excitation frequencies and for droplets situated near (but not precisely at) a PN. Details on these findings may be found in Sevilla, et al.[1]

A discovery by our group early in this AFOSR grant period is that, while at moderate amplitudes of acoustic excitation the deflected, perturbed diffusion flames surrounding the burning droplet in the vicinity of a PN undergo Sustained Oscillatory Combustion (SOC), at higher amplitudes of acoustic excitation the flames

can experience periodic partial extinction and reignition (PPER). PPER can actually persist for long periods of time, for many minutes during exposure to acoustic perturbations, depending on the fuel and other specific features. Details on these experiments are documented in a recent journal paper[2] as well as an earlier conference paper[7]. PPER phenomena are apparent through the above-noted phase-locked OH* chemiluminescence imaging, and cause a local (spatial and temporal) minimum in I' to occur at temporal peaks in pressure, resulting from the periodic extinction. CH* chemiluminescence imaging has provided the same qualitative results. As an example, oscillatory flame and droplet images for pure ethanol fuel situated near a pressure node (wavelength-based location $x/\lambda = -0.029$), for excitation at 332 hz and at two different amplitudes of excitation, are shown in **Figures 2ab**. For this particular set of excitation conditions for ethanol, a maximum pressure amplitude of 150 Pa (**Fig. 2a**) creates continuously burning, oscillatory flames (hence SOC) over many acoustic cycles, while a maximum amplitude of 222 Pa (**Fig. 2b**) creates repeatable cycles whereby the flame periodically locally extinguishes in the vicinity of the stagnation region, but then reignites at a different portion of the cycle (hence PPER). As noted above, the cyclical variation in *I'* and *p'* (as well as the horizontal flame standoff distance, δ_f), will be different between the SOC conditions and PPER conditions, as shown in corresponding plots over 3 phase-locked cycles in **Figs. 2c and 2d**, respectively. As noted above and in Sevilla, et al.[1], at the moderate excitation amplitude resulting in flame oscillations shown in **Fig. 2a**, *I'* and *p'* oscillate in phase (**Fig. 2c**), creating a positive Rayleigh index for the conditions shown. But clearly, when the flame is locally extinguished during a portion of the acoustic cycle at high amplitude excitation (e.g., acoustic phases 72° and 144° in **Fig. 2b**), the periodic reduction in OH* chemiluminescence intensity, coinciding nearly with a peak in the pressure perturbation causes *I'* and *p'* to oscillate at least partly out of phase (**Fig. 2d**).

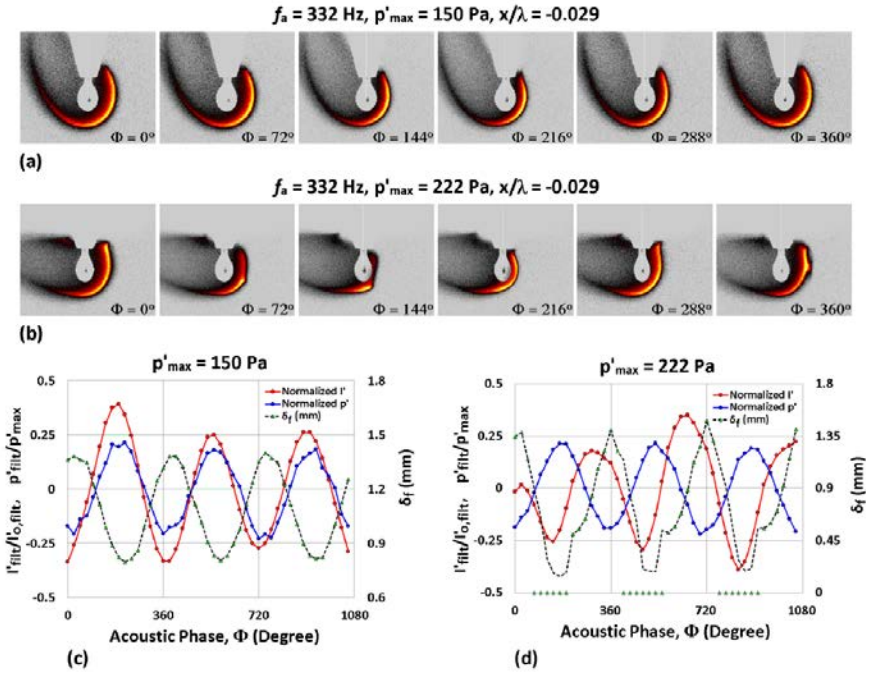

Figure 2: Instantaneous OH* chemiluminescence images of burning ethanol droplets situated at 0.029 wavelengths to the left of the PN during acoustic forcing at 332 Hz for (a) p'_{max} = 150 Pa and (b) 222 Pa. Nondimensionalized measurements of local *p'*, integrated chemiluminescent intensity *I'* and local flame standoff distance δ_f are plotted as a function of the acoustic phase for the same forcing conditions, at (c) p'_{max} = 150 Pa and (d) 222 Pa.

The differences in cyclical variation in *I'* and *p'* between conditions creating continual oscillatory combustion and PPER naturally create differences in the Rayleigh index *G(x)*. Our group has quantified a variety of features associated with PPER, including regimes in which it is observed (for ethanol and for other fuels such as JP-8), and implications for variations in burning rates and Rayleigh indices. Variations in *G(x)* for ethanol droplet combustion, for example, for a range of amplitudes of excitation and scaled locations x/λ relative to the pressure node, for three different applied frequencies, are shown in **Figure 3**. While for 332 Hz forcing, pressure perturbation amplitudes above 200 Pa create PPER (denoted by the negative values of *G(x)* shown by the x's in **Fig. 3a**), at 586 Hz, the amplitude has to rise to 235 Pa to create conditions where PPER is observed (seen in **Fig. 3b**), and at 898 Hz, the amplitude must be at 275 Pa or above (**Fig. 3c**). Clearly, for a given fuel the PPER phenomenon has a strong dependence on acoustic time scales in terms of the flame response to applied forcing. Subsequent studies with JP-8 and liquid synthetic fuel derived via the Fischer-Tropsch (FT) process indicate the presence of PPER, but at lower pressure amplitudes than are observed for ethanol.

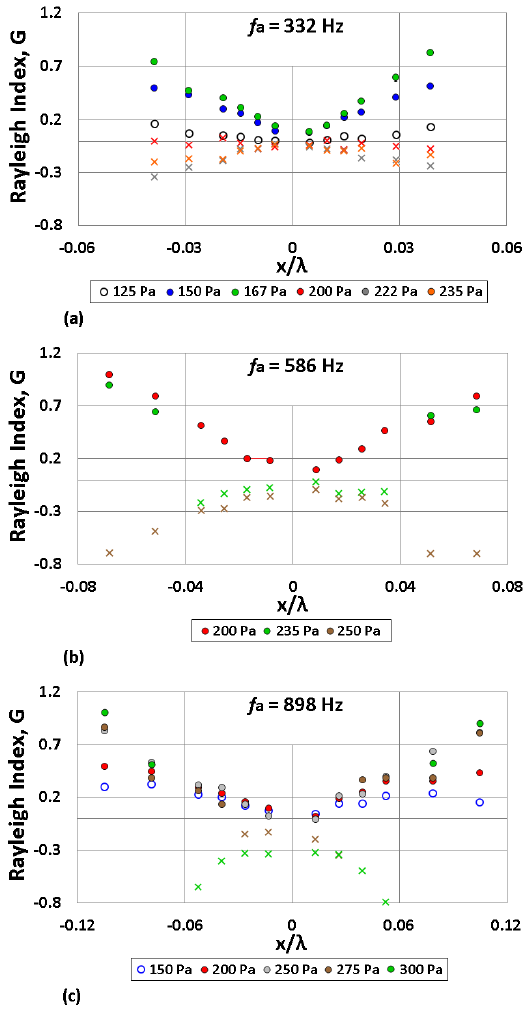

Figure 3: Rayleigh index *G* as a function of the ethanol droplet displacement x/λ at forcing frequencies (a) 332 Hz, (b) 586 Hz and (c) 898 Hz. Depending on the acoustic forcing conditions (frequency and amplitude), the burning fuel droplet is characterized by weakly oscillating flame behavior (open circles), oscillatory flame motion (filled circles) or periodic partial extinction (x).

Other features of droplet combustion characteristics during oscillatory flame motion vs. PPER have been quantified, for example, burning rate constants K, which are generally observed to increase with the amplitude of excitation, even in the presence of PPER (again, due to timescales associated with evaporative processes as compared with acoustic timescales). The phenomena associated with PPER are interpreted in terms of mean and oscillatory strain rates that impact the behavior of the deflected flame. It appears that a necessary but perhaps not sufficient condition for PPER to occur is for the oscillatory component of the normal strain field to exceed the mean component of strain. Again, this feature is dependent on the fuel (and hence reaction timescales) and is still under exploration. But overall we are able to determine maps of the sort shown in **Figure 4,** where there are excitation conditions for which the flame can undergo PPER before being forced at so high an amplitude that full extinction takes place. As indicated in **Fig. 3**, at lower applied frequencies of excitation in the waveguide, PPER first occurs at a lower amplitude than at higher frequencies, and this behavior is quantitatively somewhat different for different fuels. A remarkable observation from Figure 4 is that JP-8 and FT fuels are not only less resistant to PPER and extinction via acoustic perturbation, but they produce nearly identical results to one another, suggesting that their thermodynamic similarity as well as the dynamics associated with their combustion processes renders the same type of response to acoustic perturbation. This is a useful finding when examining the replacement of kerosene-types of fuels in propulsion systems with a synthetic fuel such as FT. Details on these and related features of PPER phenomena may be found in Bennewitz, et al.[2].

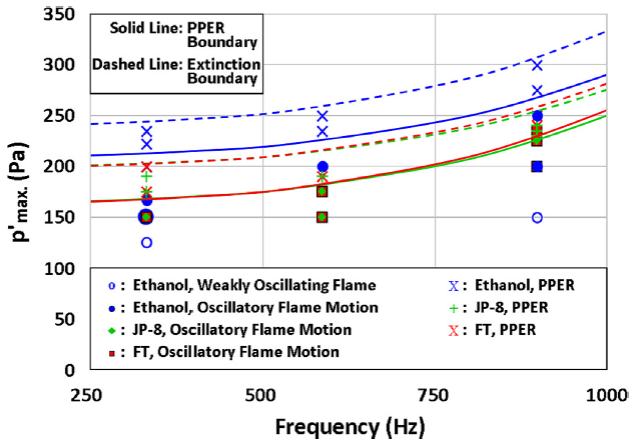

Figure 4: Periodic partial extinction boundary for ethanol, JP-8, and FT fuels. The burning droplet considered here was situated at similar relative positions close to the PN, i.e., x/λ = -0.029 for 332 Hz and x/λ = -0.026 for 586 Hz and 898 Hz.

Effects of Nano Aluminum and Nano Silica Additives on Quiescent Droplet Combustion

Another focus of our experiments under AFOSR support has been on the effect of particulate additives on liquid fuel combustion, in the absence of acoustic perturbations, in order to quantify baseline combustion behavior for nanofuels. The early part of these studies focused on ethanol fuel with either energetic particles (nano Aluminum, nAl) or inert particles (nano Silica, $nSiO_2$), and on several alternative fuel delivery methods shown in **Figure 1(b)**, as a means of comparing results from continuous fuel delivery experiments (necessary for acoustically-coupled, phase-locked imaging over relatively long periods of time) with more commonly performed fiber-suspended[8,9] or falling[10] non-fed droplet combustion experiments. These extensive studies on nanofuel droplet combustion in a quiescent environment were recently documented in a recent journal paper[11]. These studies have been particularly valuable in that other groups' experiments

on the influence of nanoparticle additives on burning fuel droplets demonstrate somewhat differing trends. While there are studies showing substantial increases in droplet burning rate constant K with nAl additives[9], other studies show much more modest increases[7] or even reductions in K with the addition of nAl[12]. The present studies of burning nanofuel droplets in a quiescent environment are designed to be systematic, controlled studies such that differences in burning characteristics could be accurately quantified.

Simultaneous visible and intensified UV images enable us to determine the burning rate constant (K) as well as flame dynamics via OH* chemiluminescence imaging. Sample results for these simultaneous images as a function of time are shown in **Figure 5**, for the two different particle additives and for two sample fuel delivery methods (Case I, non-fed, and Case III, fed). There is evidence of particulate agglomeration and expulsion from the droplet at later times in the combustion process for both non-fed and continuously fed droplets, and in both cases data taken after these expulsion events are not included in the determination of burning rate constant.

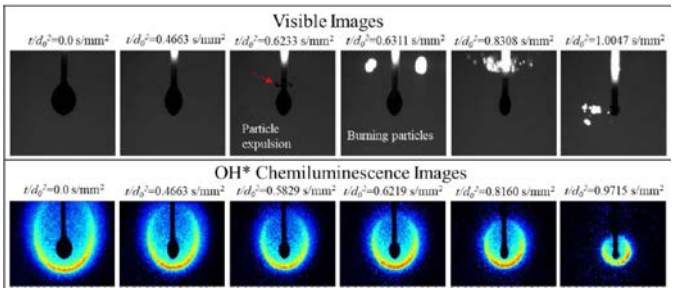

(a) Case I, 3 wt.% nAl

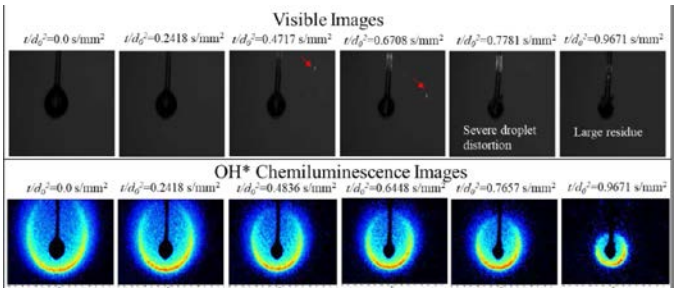

(b) Case I, 3 wt.% nSiO2

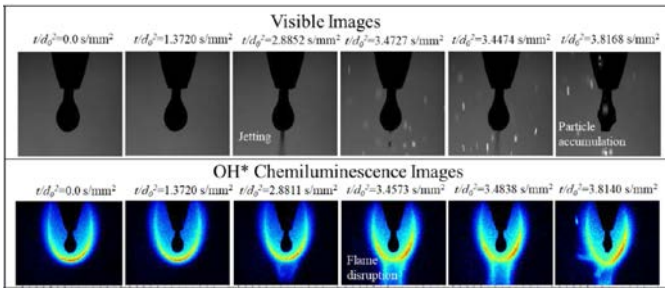

(c) Case III, 3 wt.% nAl

Figure 5. Burning sequences from visible and OH* chemiluminescence imaging for a single ethanol droplet with various loading concentrations of particles and two different methods for fuel delivery.

A simple droplet combustion model was developed to better understand the mechanisms for enhancement in K for nanofuels. We incorporate the theoretical burning rate constant (K_0) for a single droplet from the following relation[3]:

$$K_{0=}\frac{8\lambda_{\mathrm{g}}}{C_{\mathrm{p,g}}\rho_l}\ln(1+B) \qquad (4)$$

where λ_g, $C_{p,g}$, and ρ_l denote the average thermal conductivity, specific heat of the fuel and oxidizer in the gas phase, and the density of fuel (here, ethanol) at the boiling point, respectively. B is the transfer number given by

$$B = \frac{C_{p,g}(T_\infty - T_{boil}) + q/i}{h_{fg}} \qquad (5)$$

in which h_{fg} is the latent heat of vaporization of the fuel at the boiling point, T_∞ is the ambient temperature, T_{boil} is the boiling temperature of the ethanol droplet, q is the heat of combustion of fuel, and i is the stoichiometric oxygen to fuel mass ratio. To incorporate the effects of nanoparticulates in this droplet combustion model, all properties in eqn. (3) were determined for the present nanofuels with various nanoparticle types and loading concentrations using the following equations[13]:

$$\frac{\lambda_{nf}}{\lambda_{bf}} = 1 + \frac{3(\alpha-1)\varphi}{(\alpha+2)-(\alpha-1)\varphi} \qquad (6)$$

$$\rho_{nf} = (1-\varphi)\rho_{bf} + \varphi\rho_{np} \qquad (7)$$

$$C_{p,\ nf} = \frac{(1-\varphi)\rho_{bf}C_{p,\ bf} + \varphi\rho_{np}C_{p,np}}{\rho_{nf}} \qquad (8)$$

Here α is the thermal conductivity ratio between the NP and the base fuel, while φ is the volume fraction of NP within the liquid..

From the experimental imaging such as those shown in **Figure 5**, one can extract, prior to significant disruption, average burning rates K for a range of experimental conditions involving ethanol nanofuels. **Figure 6** provides a systematic summary of the variation in K as a function of particulate loading concentration for both nAl and nSiO2, and for several alternative experimental methods. While the fed droplet experiments (Case III) did appear to have systematically higher burning rate constants with nAl additives than for non-fed cases, the effects of continual fuel delivery were not significantly different from theoretical predictions for variation in K with nAl loading concentration.

The addition of nAl appeared to yield a systematic increase in K, by up to 13%, and increasing loading concentrations led to changes in droplet combustion dynamics. As observed in **Figure 5**, flow instabilities, including liquid jetting and altered droplet deformation, were observed, creating unsteady combustion when the nAl-laden droplet was continuously fed via a quartz capillary. In contrast, the addition of $nSiO_2$ showed relatively small changes in K, possibly only as large an increase as 5%, with a lack of consistent trends for increasing $nSiO_2$ concentration for different fuel delivery methods, in part due to formation of large residual shell-like structures in the later stages of combustion. The nanofuel droplet combustion model suggests that possible enhancement mechanisms for K are related to alterations in thermal conductivity with different particles as well as flame temperature with the additives. SEM and TEM images of particulate residue

revealed further differences in morphology and residue constituents after combustion; combustion completeness increased for higher nAl loading concentrations, as documented in detail in the paper[11].

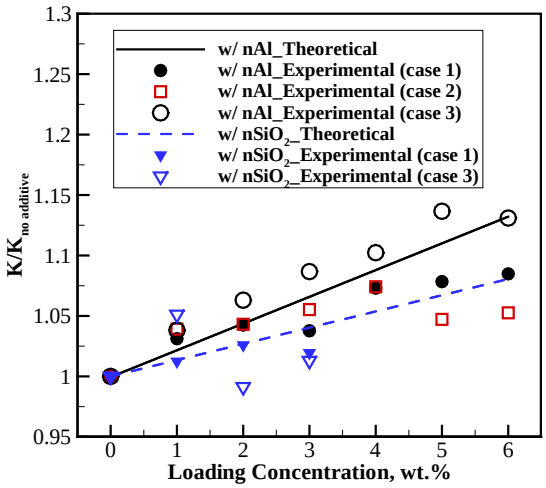

Figure 6. Comparison of K values for theoretical calculations and experimental measurements (from cases I-III) for burning nAl- and nSiO2-laden ethanol droplets at various particle concentrations.

Effects of Energetic Nanoparticulates on Acoustically-Coupled Liquid Fuel Droplet Combustion

A main emphasis in recent experiments with nAl particulates has been on the acoustically coupled nanofuel droplet combustion problem, where flame response, burning rates, and flame dynamics have a dependence on not only applied acoustics but also on the particle loading concentration. For nAl-laden ethanol droplets, extensive results for the influence on flame response to acoustic excitation are documented in a recent journal paper[14]. A separate study on sooting liquid fuels (n-dodecane and FT fuels), which require surfactants in suspending nanoparticulates, has also been conducted and is documented in a recent conference paper[15]. These results are summarized here.

Figure 7a shows simultaneous phase-locked OH* and visible imaging of 3.0 wt% nAl-laden ethanol fuel droplet combustion during acoustic forcing at a moderate pressure amplitude (that is, the pressure amplitude measured at the closest pressure antinode to the waveguide center), 167 Pa, demonstrating sustained oscillatory combustion (SOC). In contrast, **Figure 7b** shows the same kind of images but at a higher amplitude of excitation, 222 Pa, creating conditions for PPER. Remarkably, during exposure to acoustic excitation at either amplitude, the ethanol droplets with nAl additives burned for much longer periods of time (over 100 seconds) than in the absence of acoustics (around 20 seconds). For the former, there was a clear delay in particle expulsions, likely resulting from delays in the aggregation of particulates. As with neat fuels[1,2], increasing acoustic excitation amplitude is documented to increase burning rate constants K, and as shown in **Figures 8ab** for two different forcing frequencies, there can be a small increase in K when there is nAl present, especially at low loading concentrations, e.g., 1 wt.%. But more interesting is the fact that the presence of energetic nanoparticles actually increases the Rayleigh index as compared with neat fuels under the same forcing conditions, as shown in **Figures 9ab**. In the case of forcing conditions that create PPER conditions with neat fuels, the additives can increase I' and delay the onset of PPER, to the extent that the Rayleigh index becomes positive and full extinction is delayed.

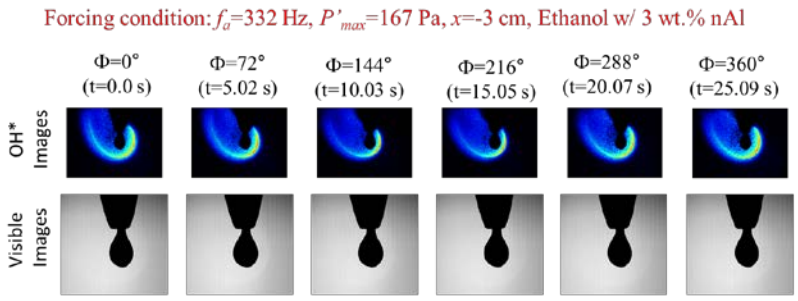

(a) Pressure amplitude p'$_{max}$ = 167 Pa

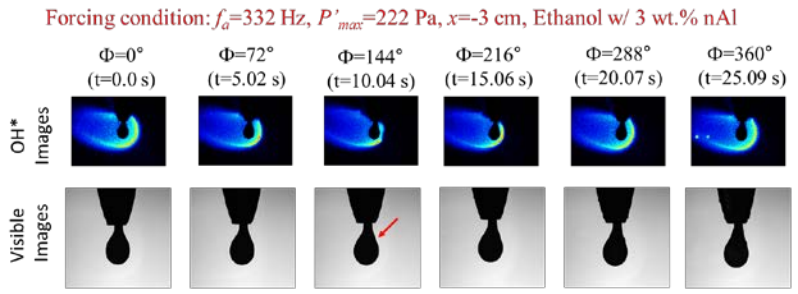

(b) Pressure amplitude p'$_{max}$ = 222 Pa

Figure 7. Phase-locked OH* chemiluminescent and visible images of ethanol with 3wt% nAl: (a) Sustained Oscillatory Combustion (SOC) at p'$_{max}$ =167 Pa; (b) Periodic Partial Extinction and Reignition (PPER) at p'$_{max}$ =222 Pa (forcing frequency f_a=332 Hz, location x=-3 cm).

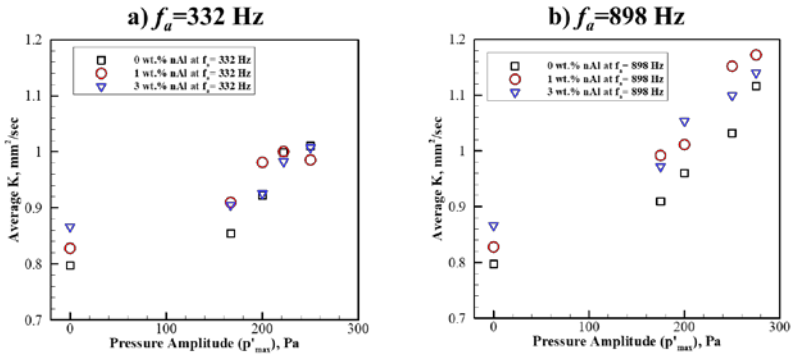

(a) (b) (c)

Figure 8: Variation in combustion parameters with pressure excitation amplitude p'$_{max}$: (a) average K at forcing frequency f_a = 332 Hz; (b) average K at forcing frequency f_a = 898 Hz. Results for neat ethanol and ethanol with 1 wt% and 3 wt% nAl, with the droplet located at x = -3 cm, are shown.

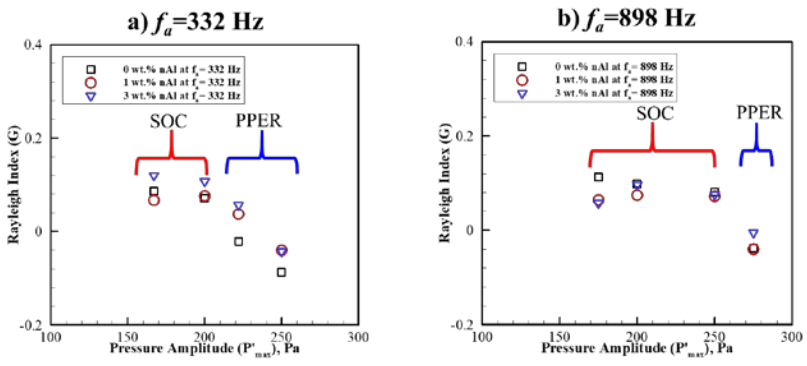

Figure 9: Local Rayleigh index G(x) variation with pressure excitation amplitude p'$_{max}$ for: (a) f_a = 332 Hz and (b) f_a = 898 Hz. Results for neat ethanol and ethanol with 1 wt% and 3 wt% nAl, with the droplet located at x = -3 cm, are shown. Here positive values of G(x) correspond to sustained oscillatory combustion (SOC) and those with negative values generally correspond to PPER phenomena.

Improved resistance to high amplitude acoustic perturbations and the associated oscillations in flame strain for nanofuels as compared with neat fuel can further be quantified in studies focusing on extinction. Nanofuel droplet experiments with systematic increases in forcing amplitude for a fixed frequency have been performed, and the conditions for which the initiation of complete flame extinction have been documented. Local strain rates experienced by the flame in the vicinity of the stagnation region may be estimated from local acoustic conditions as described in Sevilla, et al.[1] and Bennewitz, et al.[2] The estimated variation in mean extinction strain rate for ethanol with increasing nAl loading concentration is shown, for example, in **Figure 10**. There is not as significant a change in the oscillatory strain rate, however, also as shown. Yet increases in mean extinction strain rate are quite remarkable, and could have attendant benefits in LRE applications.

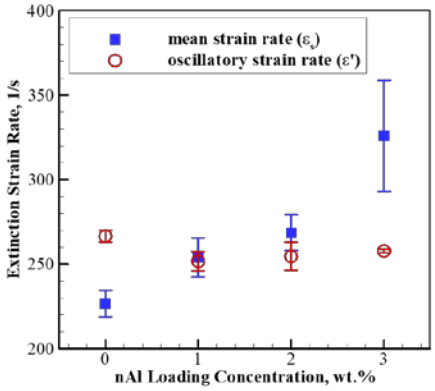

Figure 10. Estimated extinction strain rate as a function of wt% of nAl additive in the nanofuels, for 332 Hz acoustic excitation of burning droplets in the vicinity of the pressure node (velocity antinode).

Finally, additional experiments have been performed in the past year on alternative sooting hydrocarbon fuels, n-dodecane and Fischer-Tropsch (FT) liquid synfuel, with 80 nm reactive nAl partible additives. For these fuels, surfactant (Span80) was required to maintain a uniform dispersion of nanoparticles. Both

Span80 and nAl concentrations impacted droplet combustion behavior, with and without the application of acoustic excitation. For example, burning rate constants for nanofuel dodecane in the absence of acoustics can increase with increasing Span80 or nAl concentration, as shown in **Figure 11**.

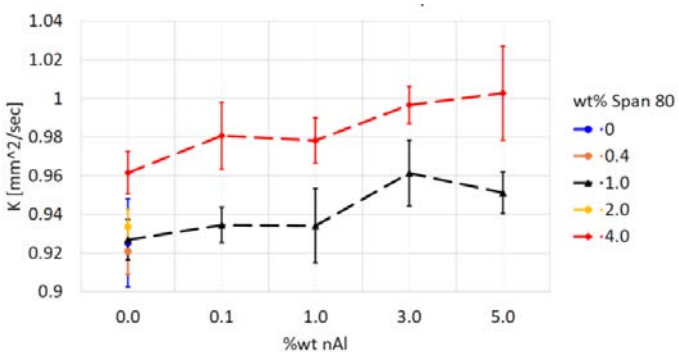

Figure 11. Variation in burning rate constants for n-dodecane with various concentrations of Span80 and nAl.

There are additional differences in the behavior of these acoustically-coupled nanofuel combustion processes and the earlier studies with ethanol. For example, for the case with 1 wt% Span-80 and 3 wt% nAl, visible images in **Figure 12** show occasional particle ejection and burning at early times, and in some instances the intensity and frequency of these events becomes more severe as the droplet shrinks because the effective additive concentration increases. Vigorous microexplosions were observed near the end of droplet combustion and residue buildup was often seen after burnout.

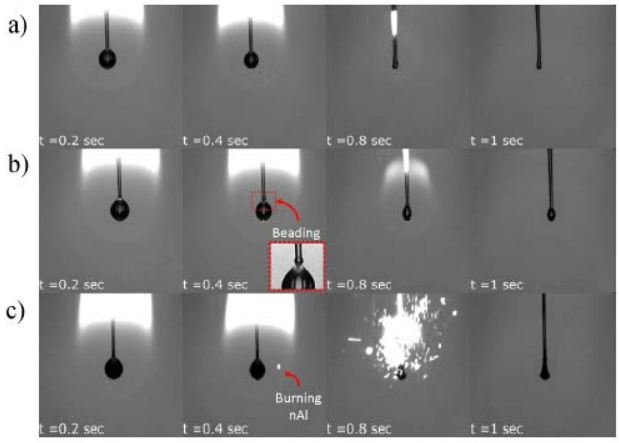

Figure 12. High-speed visible imaging of nanofuel droplet combustion: (a) neat dodecane; (b) dodecane with 4 wt% Span-80 only, where liquid beading forms above the droplet; (c) dodecane with 1 wt% Span-80 and 3 wt% nAl, where microexplosions and solid particulate residue were observed at the end of combustion.

Finally, **Figure 13** shows the results of the variation in burning rate constant for the Fischer-Tropsch nanofuel droplets, with and without acoustic excitation. Here the droplets could experience sustained combustion even at forcing amplitudes of 150 Pa, the case shown in Figure 5. While there are similar overall behaviors noted for FT fuels with Span-80 and nAl additives as compared with dodecane, there was always a systematic increase in K with acoustic excitation over the quiescent cases, whether one examined neat fuel, FT with Span-80 alone, or FT with Span-80 and nAl. The slightly higher K values observed for FT

droplets situated closer to the pressure node (x/λ = 0:0097) that further away from the PN (x/λ = 0:029) was consistent with the fact that a higher velocity perturbation altering flame dynamics and strain rates occurs near a PN. These and other findings are documented in Vargas, et al.[15]

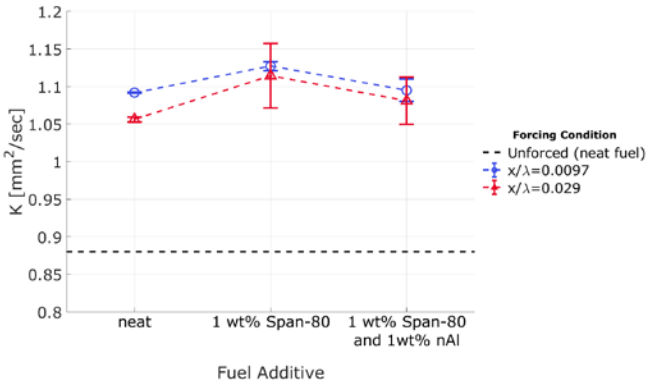

Figure 13. Burning rate constant for Fischer-Tropsch nanofuel droplets with acoustic forcing amplitude corresponding to p'_{max} = 150Pa, f_a = 332 Hz and droplet locations x/λ = 0.0097 and 0.029.

A new direction in our research has involved exploration of single and multiple gaseous fuel injectors in our acoustic waveguide, where flame structures experience natural interactions and instabilities and where these instabilities can be altered in response to applied acoustic disturbances. Additional recent experiments have explored the effect of acoustics on reactive flow emanating from multiple (three) fuel injectors adjacent to one another within the waveguide, in addition to a coaxial injection configuration. In the presence of a standing acoustic wave near a pressure node (velocity antinode), because of the long wavelength acoustic disturbance in relation to the sizes of the injectors, there appears to be relatively limited coupling or interaction at all among the reactive shear layers in the 3-injector case in response to transverse acoustic perturbations. Ongoing experiments at UCLA and at AFRL seek to understand the dynamics of this and other configurations involving gaseous reactants, in both atmospheric and elevated pressure chambers, as a baseline for future multiphase flow reactive experiments relevant to combustion instabilities in LREs.

Bibliography: UCLA Publications and Presentations during the AFOSR grant period

Journal papers

- Bennewitz, J., Valentini, D., Plascencia, M., Vargas, A., Sim, H. S., Lopez, B., Smith, O. I., and Karagozian, A. R., "Periodic Partial Extinction in Acoustically Coupled Fuel Droplet Combustion", ***Combustion and Flame,*** Vol. 189, pp. 46-61, 2018.
- Sim, H. S., Plascencia, M. A., Vargas, A., Bennewitz, J. W., Smith, O. I., and Karagozian, A. R., "Effects of Inert and Energetic Nanoparticles on Burning Liquid Ethanol Droplets", ***Combustion Science and Technology,*** 2018. DOI: 10.1080/00102202.2018.1509857**.**
- Sim, H. S., Plascencia, M. A., Vargas, A., and Karagozian, A. R., "Acoustically-Forced Droplet Combustion of Liquid Fuel with Reactive Aluminum Nanoparticulates", ***Combustion Science and Technology***, 2019. DOI: https://doi.org/10.1080/00102202.2019.1593971

Conference papers

- Bennewitz, J., Plascencia, M., Vargas, A., Valentini, D., Smith, O. I., and Karagozian, A. R., "Periodic Partial Extinction in Acoustically Coupled Fuel Droplet Combustion", 24th International Congress of Theoretical and Applied Mechanics, Montreal, Canada, August, 2016.
- Sim, H. S., Plascencia, M., Vargas, A., Bennewitz, J., Smith, O. I., and Karagozian, A. R., "Effects of Aluminum Nanoparticle Additives on Liquid Fuel Droplet Combustion with and without Acoustic Excitation", Paper 3C09, 10th U.S. National Combustion Meeting, Univ. of Maryland, April, 2017.
- Vargas, A., Sim, H. S., Plascencia, M., and Karagozian, A. R., "Effect of aluminum nanoparticle additives on sooting hydrocarbon fuel droplet combustion", Paper 3G04, 11th U.S. National Combustion Meeting, Pasadena, California, March, 2019.

Conference presentations (abstract only)

- John Bennewitz, Miguel Plascencia, Andres Vargas, Dario Valentini, Owen I. Smith and Ann R. Karagozian, "Periodic Partial Extinction Boundary for Acoustically Coupled Ethanol Droplet Combustion", presented at the 10th Southern California Symposium on Flow Physics, UC Irvine, April 9, 2016.
- Plascencia, M., Bennewitz, J., Vargas, A., Sim, H.-S., Smith, O. and Karagozian, A. R., "Periodic Partial Extinction Regime in Acoustically Coupled Fuel Droplet Combustion", presented at the American Physical Society/Division of Fluid Dynamics Meeting, Portland, OR, November, 2016.
- Sim, H. S., Plascencia, M., Vargas, A., Bennewitz, J., Smith, O. I., and Karagozian, A. R., "Effects of Particle Additives on Acoustically Coupled Liquid Fuel Droplet Combustion", presented at the American Physical Society/Division of Fluid Dynamics Meeting, Portland, OR, November, 2016.
- Sim, H. S., Plascencia, M., Vargas, A., Bennewitz, J., Smith, O. I., and Karagozian, A. R., "Effects of Aluminum Nanoparticle Additives on Liquid Fuel Droplet Combustion with and without Acoustic Excitation", presented at the 10th U.S. National Combustion Meeting, Univ. of Maryland, April, 2017.
- Andres Vargas, Hyungsub Sim, Miguel A. Plascencia, Owen I. Smith and Ann R. Karagozian, "Effects of Aluminum Nano Particles on Burning Liquid Fuel Droplets in a Quiescent Environment", presented at the 11th Southern California Symposium on Flow Physics, UC San Diego, April 22, 2017.
- Miguel A. Plascencia, Hyungsub Sim, Andres Vargas, Owen I. Smith and Ann R. Karagozian, "Effects of Aluminum Nano Particles on Acoustically Coupled Droplet Combustion", presented at the 11th Southern California Symposium on Flow Physics, UC San Diego, April 22, 2017.
- Miguel A. Plascencia, Hyungsub Sim, Andres Vargas, Owen I. Smith and Ann R. Karagozian, "Effects of Energetic and Inert Nano Particles on Burning Liquid Ethanol Droplets", presented at the American Physical Society/Division of Fluid Dynamics Meeting, Denver, CO, November, 2017.
- Andres Vargas, Hyungsub Sim, Miguel A. Plascencia, Owen I. Smith and Ann R. Karagozian, "Effects of Nanoparticulate Additives on Acoustically-Coupled Fuel Droplet Combustion", presented at the American Physical Society/Division of Fluid Dynamics Meeting, Denver, CO, November, 2017.

- Hyungsub Sim, Miguel A. Plascencia, Andres Vargas, Owen I. Smith and Ann R. Karagozian, "Effects of Inert and Energetic Nanoparticles on Burning Liquid Ethanol Droplets", presented at the 12th Southern California Symposium on Flow Physics, USC, April, 2018.
- Andres Vargas, Hyungsub Sim, Miguel A. Plascencia, Owen I. Smith and Ann R. Karagozian, "Acoustically-Driven Combustion Dynamics and Extinction in Burning Nanofuel Droplets", presented at the American Physical Society/Division of Fluid Dynamics Meeting, Atlanta, GA, November, 2018.
- Vargas, A., Sim, H. S., Plascencia, M., and Karagozian, A. R., "Effect of aluminum nanoparticle additives on sooting hydrocarbon fuel droplet combustion", presented at the 11th U.S. National Combustion Meeting, Pasadena, California, March, 2019.

Student Ph.D. prospectus documents (for Ph.D. candidacy)

- Plascencia, M., "Combustion of Liquid Nanofuels and Reactive Processes in Liquid Rocket Engines", Ph.D. prospectus, March, 2018.
- Vargas, A., "Acoustically Coupled, Non-Premixed Combustion Processes", Ph.D. prospectus (in progress), May, 2019.

References

[1] Sevilla-Esparza, C. I., Wegener, J. L., Teshome, S., Rodriguez, J. I., Smith, O. I., and Karagozian, A. R., "Droplet Combustion in the Presence of Acoustic Excitation", ***Combustion and Flame***, Vol. 161, pp. 1604-1619, 2014.

[2] Bennewitz, J., Valentini, D., Plascencia, M., Vargas, A., Sim, H. S., Lopez, B., Smith, O. I., and Karagozian, A. R., "Periodic Partial Extinction in Acoustically Coupled Fuel Droplet Combustion", ***Combustion and Flame,*** Vol. 189, pp. 46-61, 2018.

[3] Law, C. K. 1982. Recent advances in droplet vaporization and combustion. ***Prog. Energy Combust. Sci.***, **8**(3), 171–201.

[4] Dattarajan, S., Lutomirski, A., Lobbia, R., Smith, O. I., and Karagozian, A. R., "Acoustic Excitation of Droplet Combustion in Microgravity and Normal Gravity", ***Combustion and Flame***, Vol. 144, Issues 1-2, pp. 299-317, January, 2006.

[5] Tanabe, M. Morita, T., Aoki, K., Satoh, K., Fujimori, T., Sato, J., ***Proc. Combust. Inst***. 28, 1007–1013, 2000.

[6] Rayleigh, Lord, "The explanation of certain acoustical phenomena", ***Nature*** 18, pp. 319-321, 1878. doi:http://dx.doi.org/10.1038/018319a0.

[7] Bennewitz, J., Plascencia, M., Vargas, A., Valentini, D., Smith, O. I., and Karagozian, A. R., "Periodic Partial Extinction in Acoustically Coupled Fuel Droplet Combustion", 24th International Congress of Theoretical and Applied Mechanics, Montreal, Canada, August, 2016.

[8] Pfeil, M. A., "Changes in combustion behavior of liquid fuels due to the addition of small amounts of ammonia borane or nano aluminum", M.S. Thesis, Purdue University, 2012.

[9] Pfeil, M. A., Rosen, S. C., Yu, Y. C., Anderson, W. E., and Son, S. F., "Effects of NanoAluminum on Droplet Combustion and Combustion Instabilities in a Single Element Rocket Combustor", AIAA Paper 2010-7154, 46th AIAA/ASME/SAE/ASEE Joint Propulsion Conference & Exhibit, 25 - 28 July 2010.

[10] Tanvir, S. and Qiao, L, "Effect of Addition of Energetic Nanoparticles on Droplet-Burning Rate of Liquid Fuels", ***J. Propulsion Power***, Vol. 31, No. 1, January–February 2015.

[11] Sim, H. S., Plascencia, M. A., Vargas, A., Bennewitz, J. W., Smith, O. I., and Karagozian, A. R., "Effects of Inert and Energetic Nanoparticles on Burning Liquid Ethanol Droplets", ***Combustion Science and Technology,*** 2018. DOI: 10.1080/00102202.2018.1509857.

[12] Guerieri, P. M., DeLisio, J. B., and Zachariah, M. R. 2017. Nanoaluminum/Nitrocellulose microparticle additive for burn enhancement of liquid fuels. ***Combust. Flame***, 176, 220–228.

[13] Li, C. H., and Peterson, G. P. 2006. Experimental investigation of temperature and volume fraction variations on the effective thermal conductivity of nanoparticle suspensions (nanofluids). ***J. Appl. Phys***., 99(8), 084314

[14] Sim, H. S., Plascencia, M. A., Vargas, A., and Karagozian, A. R., "Acoustically-Forced Droplet Combustion of Liquid Fuel with Reactive Aluminum Nanoparticulates", ***Combustion Science and Technology***, 2019. DOI: https://doi.org/10.1080/00102202.2019.1593971.

[15] Vargas, A., Sim, H. S., Plascencia, M., and Karagozian, A. R., "Effect of aluminum nanoparticle additives on sooting hydrocarbon fuel droplet combustion", Paper 3G04, 11th U.S. National Combustion Meeting, Pasadena, California, March, 2019

Final Report: Research Activities at Purdue University

William E. Anderson*, Swanand V. Sardeshmukh†, Tristan L. Fuller‡, and Arnau Pons§
Purdue University, West Lafayette, IN, 47906

Introduction

The prediction of combustion instability is very complex due to the nonlinear coupling of physical phenomena at different temporal and spatial scales such as acoustics, hydrodynamics, turbulence, and chemical kinetics. The problem becomes even more difficult in liquid rocket combustors due to unmixed propellants operating at near-stoichiometry with no diluents and high pressure. This leads to high-amplitude pressure pulses and local rates of energy addition that can approach TW/m^3 that can strongly affect the flow dynamics. This project aims to deepen our quantitative understanding of combustion instability with the ultimate goal of a-priori prediction. The present study encompasses concurrent high-fidelity simulations and experimental tests of a model combustor that exhibits self-excited instabilities that are dependent on flow and geometric parameters. Experimental observations are used to motivate a detailed study of results from validated simulations for further fundamental understanding. The primary study configuration uses a single element shear coaxial injector similar to those found in modern high-performance rocket engines, with a propellant combination of subcritical gaseous methane and warm oxygen. All experimental design and operating conditions are well-controlled so that they can be accurately and precisely represented in a simulation. The model combustor was designed to produce self-excited combustion dynamics, which is critical for representing the pressure and heat release coupling mechanics in real devices. As a part of the project experimental data were obtained from 42 test firings in which the oxidizer temperature was varied from 440 to 800 K. This report first introduces the study configuration, experiment, and the high-fidelity computational model. The experimental results and their comparisons with results from the high-fidelity CFD simulations are presented next, followed by a study on the pressure response to unsteady heat release events.

Overview of the Study Configuration

Experimental Configuration

The experiment is a model rocket combustor emulating the stability characteristics associated with a single element of an oxidizer-rich staged combustion shear coaxial injector. The core of the injector is fed by an oxidizer rich preburner, while the fuel is delivered through an annular passage concentric to the core oxidizer flow. The experimental hardware is compressed together by a hydraulic jack to allow efficient testing of model geometry changes. The propellant manifolds and injector were designed to provide injection boundary conditions with the highest confidence, while allowing for high modularity to enable studies at isolated system and flow parameters. While the preburner is ignited with a torch, the main chamber is ignited with a laser pulse at 532nm. Ignition with a laser has a number of advantages, but to name a few: no larger orifice at wall disrupting acoustics and flow, precise ignition location, robust ignition and reduced system complexity. Figure 1 is the cross-sectional view of the combustor with the acronym HAMSTER.

The preburner combusts oxygen and hydrogen at a low equivalence ratio to produce warm oxygen-rich gas with minimal amounts of water vapor. Choking the flow allows for a more accurate reproduction of the boundary conditions set in the CFD simulations and facilitates the validation of high-fidelity simulation models. The flow from the preburner is choked at the inlet to the oxidizer manifold using a plate with 169 equidistant, equally sized small holes; the plate is designed to ensure a well distributed, well formed flow. The fuel flow can be choked upstream of either manifold; the presence of a modular choke ring allows the study of the impact of the response of the fuel manifold on combustion stability in the chamber. In the current configuration, the fuel flow is choked such that the fuel manifold is isolated from downstream perturbations. The nominal design conditions for HAMSTER are shown in Table 1.

The chamber and injection recess were designed to provide high fidelity measurements in key areas within the

*Professor, School of Aeronautics and Astronautics, 701 W. Stadium Ave.
†Research staff, Maurice J. Zucrow Laboratories, 215 Chaffee Hall, 500 Allison Road
‡Ph.D. candidate, Maurice J. Zucrow Laboratories, High Pressure Laboratory, 500 Allison Road
§Ph.D. candidate, Maurice J. Zucrow Laboratories, 211 Chaffee Hall, 500 Allison Road

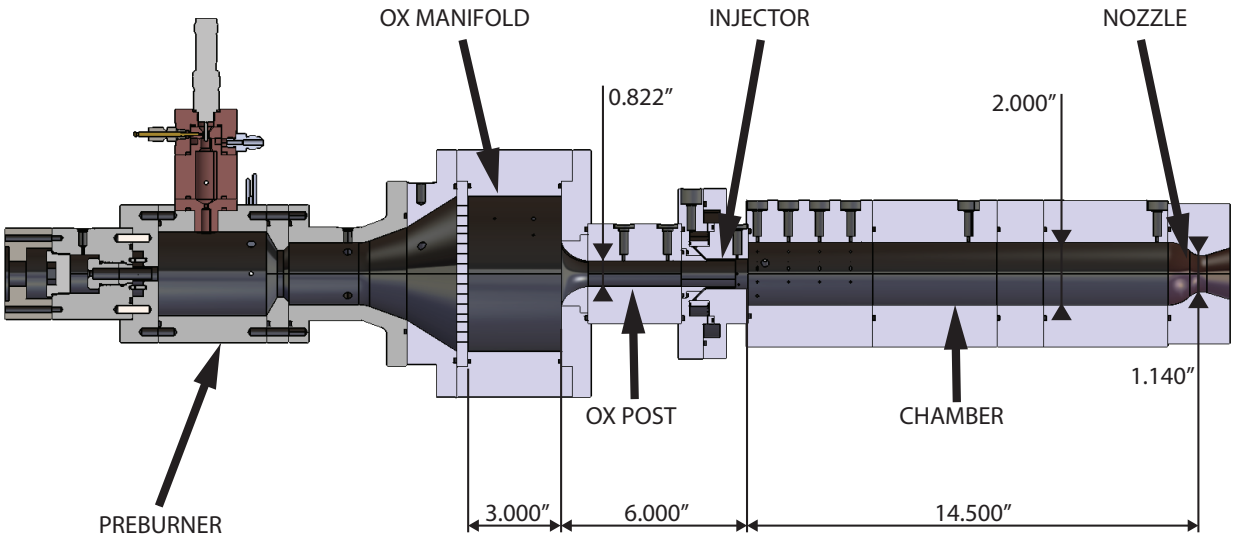

Fig. 1 Experimental setup of HAMSTER, a single shear coaxial injector element model rocket combustor.

Table 1 Main experimental parameters for HAMSTER.

Parameter	Value	Comments
Propellant Combination	CH_4/O_2	Both gaseous
Equivalence Ratio	$\phi = 0.8$	Predictable and repeatable
Propellant Temperature	Oxidizer: 440-800 K Fuel: 290-310 K	700 K nominal
Mass flow rate	Oxidizer: 0.87 lbm/s Fuel: 0.17 lbm/s	Constant for all tests at $\phi = 0.8$
Mean Oxidizer Post Mach No.	M = 0.4	
Chamber Diameter	ID = 2” = 50.8 mm	For PIV, PLIF measurements
Chamber Pressure	1.172 MPa (170 psi)	Ideal gas conditions

combustion zone, with emphasis on probing of the hydrodynamic and mixing effects on combustion and their response to acoustic perturbation. Figure 2 depicts a detailed view of the injector displaying the main locations and instrumentation in this critical area. High frequency pressure transducers were placed at axial locations spanning the distance between the oxidizer manifold distribution plate to the main chamber exhaust nozzle. More pressure transducers were placed near the head end of the chamber to better resolve the acoustic and general pressure fluctuations near the combustion zone. Additionally a high frequency pressure transducer was located azimuthally clocked 135° from another pressure transducer at the same axial location; both signals from the transducers were in phase exactly (not shown), which supports the assumption of axisymmetric behavior.

To investigate the relationship of the hydrodynamics to the injection and acoustic coupling behavior, PMTs were employed to complement the high frequency pressure transducers. The PMTs were located at the same axial locations as the high frequency pressure transducer at the head end of the combustor, as shown in Figure 2. At each axial location at the head end of the combustion chamber were a set of PMT probes: one cutting across the diameter of the chamber and two orthogonal to the first, but cutting different chords across the chamber. This is represented in Figure 3. The chord cutting probes have a number of purposes:

1) Gather information about the recirculation zone
2) Provide correlation data for the diameter cutting probe in order to determine distribution of emitters within line-of-sight integrated domain
3) Attempt to determine spatial limits of shear location, especially in the radial direction

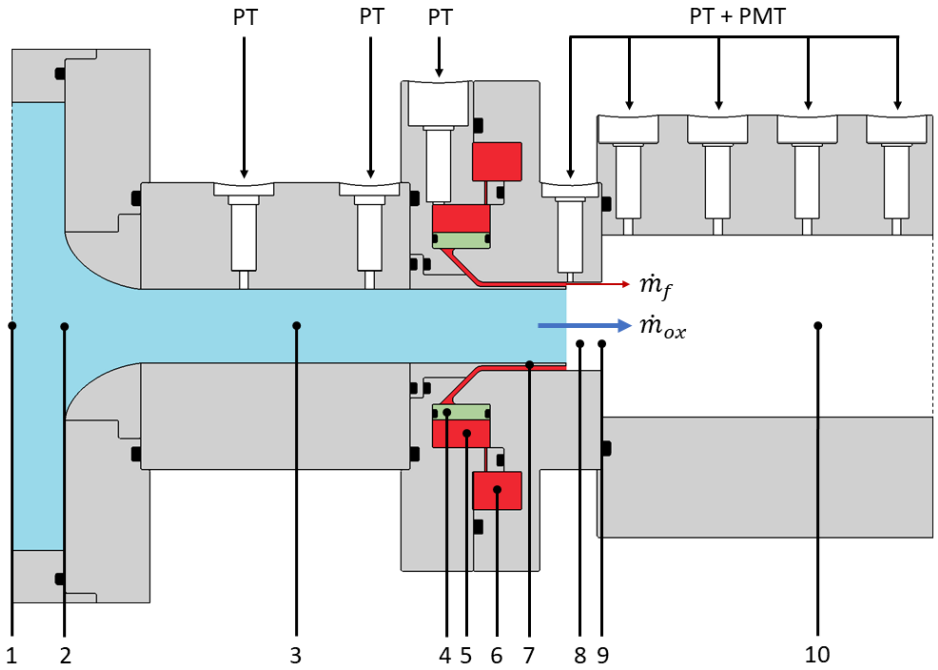

Fig. 2 Detail view of the injector design of the HAMSTER combustor. 1) Oxidizer manifold; 2) Oxidizer post inlet; 3) Oxidizer post; 4) Fuel choke ring; 5) Fuel inner manifold; 6) Fuel outer manifold; 7) Fuel collar; 8) Injector recess; 9) Dump plane; 10) Combustion chamber. In the figure "PT" refers to a high-frequency pressure transducer, and "PMT" refers to a fiber optically coupled photomultiplier detector.

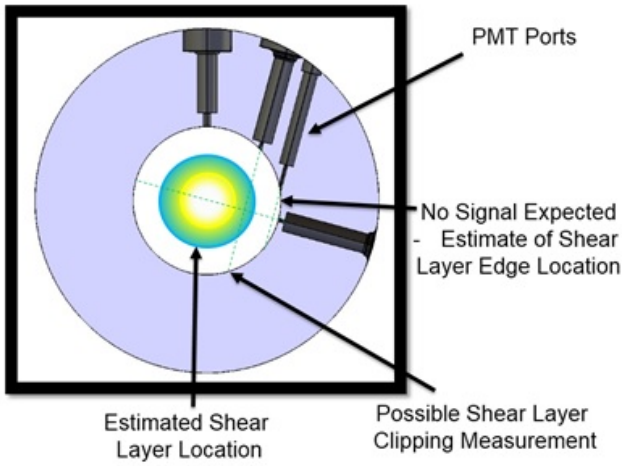

Fig. 3 Cross-sectional view of combustion chamber showing PMT probe arrangement.

Computational Modeling

The combustor is simulated as an axisymmetric configuration. This choice allows the use of advanced chemical kinetics models, which is one of the targets of the study. Computational domain representing the experimental configuration is shown in Figure 4. The computational domain includes the oxidizer manifold, oxidizer post, annular fuel passage, the combustion chamber and nozzle. The experimental arrangement insures that both the oxidizer and fuel inlets are choked along with the nozzle. These are well controlled boundary conditions to be utilized for the simulations. The nominal equivalence ratio employed in the experiments is $\phi = 0.8$.

The choked inlets allow the use of a mass flow and total temperature boundary condition. Both the quantities required for the specification of the boundary conditions are experimentally measured and utilized for the simulation.

The inner walls of the oxidizer manifold and chamber are lined with a thermal barrier coating (Yttria-stabilized Zirconia). This is consistent with an adiabatic wall condition, which is used at the wall in addition to the no-slip condition. The operation of the combustor at a low reduced pressure and high reduced temperatures implies ideal gas behavior. The structured mesh is composed of 108,291 nodes and 107,200 elements, with a typical resolution of 0.1 mm near the injector. A detailed view of the mesh around the injector recess area is shown in Figure 5. Chemical kinetics are modeled with GRI Mech 1.2 [1]. It is well suited for the purpose since the oxidizer used is pure oxygen instead of air. Predictions of ignition delay with this mechanism closely agree with the measurements as well as predictions of other mechanisms from literature [2]. With the detailed kinetics, the chemiluminescent species OH* and CH* are modeled. The time scales associated with OH* require modeling as a transported species. The CH* can be considered to be in a quasi-steady state due to its short lifespan and its concentration is calculated post-simulation.

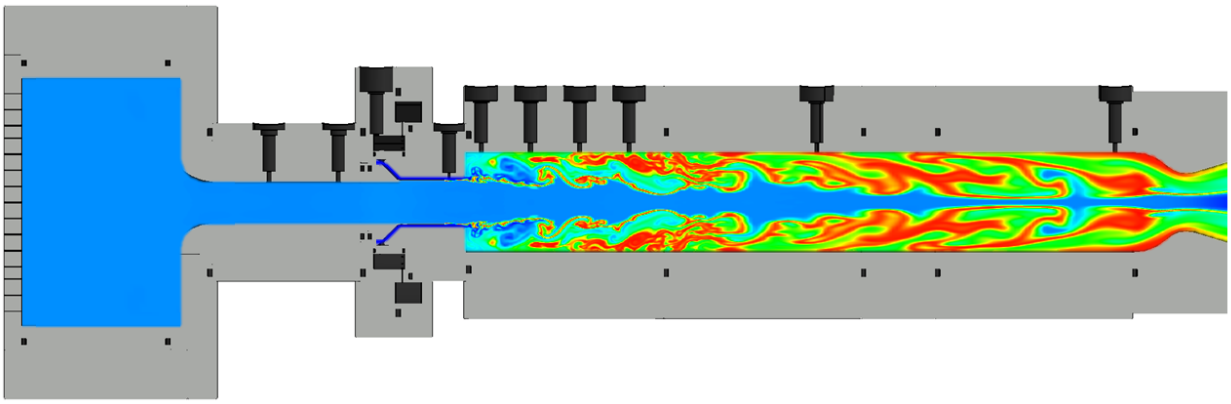

Fig. 4 Computational domain for the simulations. All simulations are two-dimensional axisymmetric.

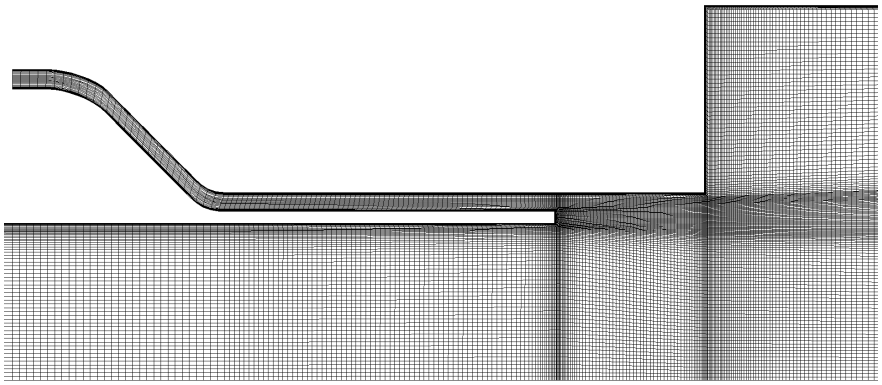

Fig. 5 Detail view of the mesh in the vicinity of the injector recess and dump plane.

The simulations are performed with Purdue's in-house code GEMS. The code GEMS is a fully coupled Navier-Stokes solver with second order accuracy in both space and time. Turbulence modeling technique- detached eddy simulations is used, which captures large scale motions are captured up to the grid length scale, while the sub-grid turbulence is modeled with a $k-\omega$ model due to Wilcox[3]. The experimental conditions are amenable to the ideal gas law and hence that is used for equation of state. The thermal and transport properties are obtained using NASA polynomial coefficients from McBride et al. [4]. The boundary conditions, fluxes and source terms are treated implicitly for the discretization. The solution of the linearized equations is obtained using line Gauss-Seidel algorithm and the approximate factorization errors are minimized by employing dual time stepping algorithm.

Overview of Results

A primary objective of the present study is the development of accurate high-fidelity models and their use to study the physics of combustion instability mechanisms in detail. A key step in attaining this objective is the validation of the CFD model. The development and use of advanced analytical techniques that support meaningful comparisons is therefore critical. In the past, many studies have only compared the pressure. Such a comparison provides a direct and quantitative assessment, subject to the accuracy of measurements and the assumptions of the models. This, however does not provide the assessment of the coupling between the heat release and the fluid dynamics in the combustor. It is one of the purposes of the current study to provide another metric relevant to the reacting flow in conjunction with the pressure for the model validation.

The oxidizer temperature is an important parameter. It affects the acoustic speed, the momentum flux ratio, injection hydrodynamics and significantly, the chemical kinetics rates. The variation of acoustic speed determines the response of various components such as the oxidizer manifold or the post, fuel annulus and the combustor. The momentum flux ratio and hydrodynamics of mixing are tied together, but apart from that, presence of geometric features such as an orifice can also affect individual propellant hydrodynamics depending on the temperature and hence momentum. The dependence of chemical kinetics on the temperature being exponential is perhaps the most notable among these, since it can change the ignition delay by order of magnitude for a difference of 100 K. This parameter is therefore the main variable of interest[5].

The experiment varied oxidizer temperature in steps from 440 K to 800 K, while the simulations were conducted for the two extremes of the oxidizer temperatures: 400 K and 730 K. The simulations were able to predict the overall thermo-acoustic behavior of the combustor with variation of the oxidizer temperature. The detailed comparison of the computational results is carried out using pressure and the flame emission measurements. Such a comparison is useful for establishing confidence in the simulation results. Although the present study demonstrates the methodology for the comparison, additional spatial resolution for the experiments and computational resources for the simulations will greatly benefit future studies for this purpose.

A. Detailed Pressure Comparisons

Figures 6 and 8 show typical pressure waveforms measured 0.3" downstream of the dump plane at low and high oxidizer temperatures, respectively. The pressure signal at the low oxidizer temperature indicates that both the experiment and simulation show modulation of the primary longitudinal mode by a low frequency chug mode. One point of difference between the experiment and the simulation is the presence of sharp spikes in the former, which are observed randomly at this temperature. The similarity in this behavior is apparent with the Power Spectral Density (PSD) plots in Figure 7. The low frequency bulk mode, the first acoustic mode and its first harmonic are seen for both the experiment and simulation. The relative amplitudes of the acoustic mode peaks are also observed to be comparable between the two. The limitation of the simulated physical time implies that the frequency resolution in the PSD plot will be lower than that of the experiment.

The pressure signal at the higher oxidizer temperature is shown in Figure 8. It shows that there is difference between the experiment and the simulation at this condition. The experimental pressure shows a periodic, steep fronted waveform, whereas the corresponding simulation has modulations of a relatively moderate amplitude peak. Although the overall pressure fluctuation magnitude is comparable, the lack of steep fronted waves in the simulations leads to difference in the PSD plot shown in Figures 7 and 9. The amplitude and spectral content of the pressure for the 400/440K oxidizer cases agree very well. The 730K oxidizer temperature case shows similar frequency content, but different dominant modes and relative amplitudes.

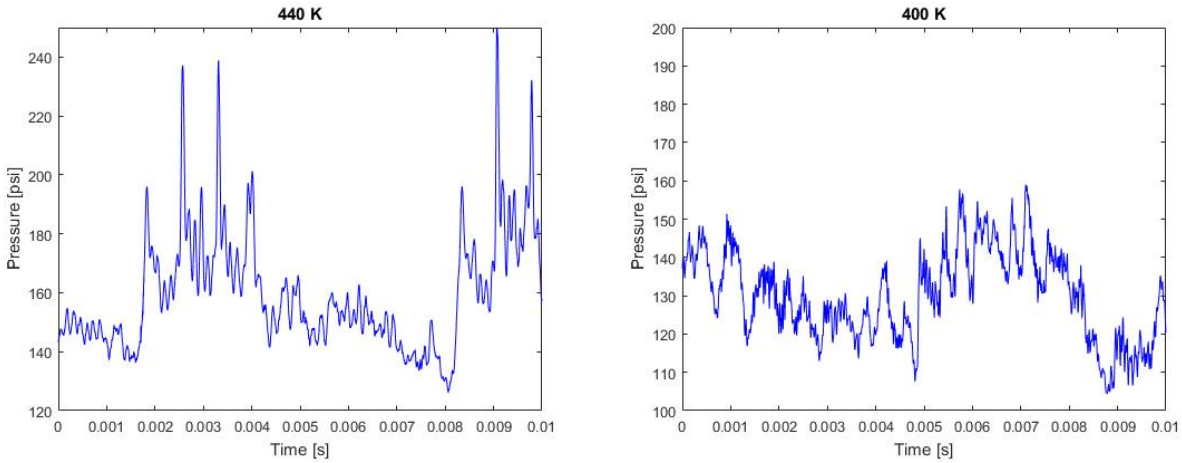

Fig. 6 Comparison of the pressure waveforms from the experiment at 440 K (L), and CFD simulation at 400 K (R). The pressure measurement is located at 0.3" downstream of the dump plane of the combustor.

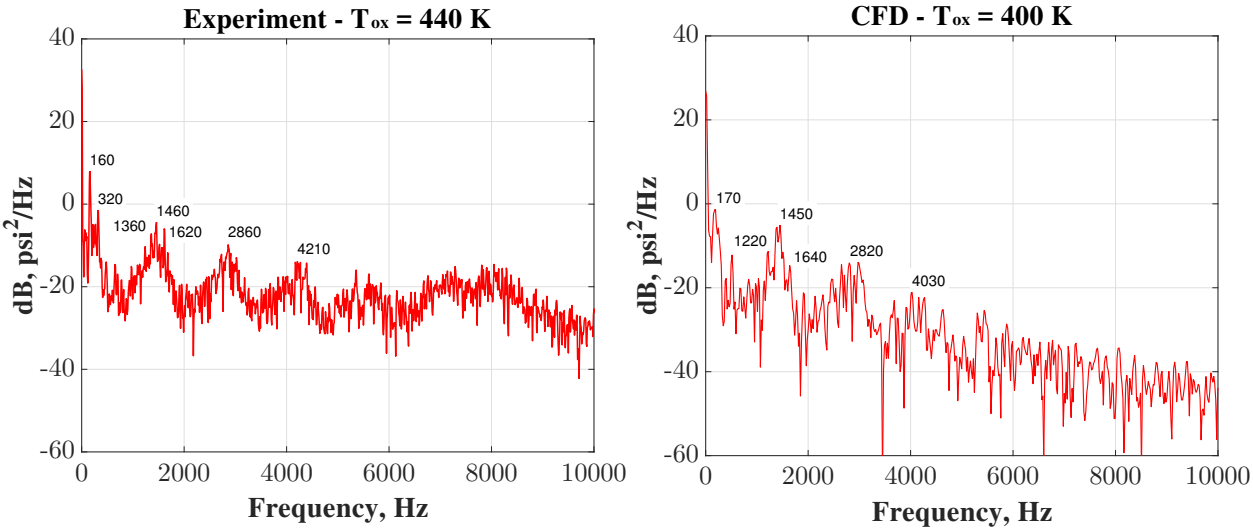

Fig. 7 Comparison of the pressure power spectral density from the experiment at 440 K (L), and CFD simulation at 400 K (R). The pressure measurement is located at 0.3" downstream of the dump plane of the combustor.

The amplitudes of the time series collected from the experiments are not always so regular, and are generally non-stationary at lower oxidizer temperatures. As the oxidizer temperature moves away from the optimal acoustic tuning temperature for the oxidizer post, the time series of the pressure and chemiluminescence become intermittent and less regular in shape. Because the CFD simulations are limited to about 60 ms of run time due to the computational cost, it may be that the simulations have not had enough time to produce a behavior that better represents the measurements. In the next sections, results from the experiments and companion simulations are discussed in more detail.

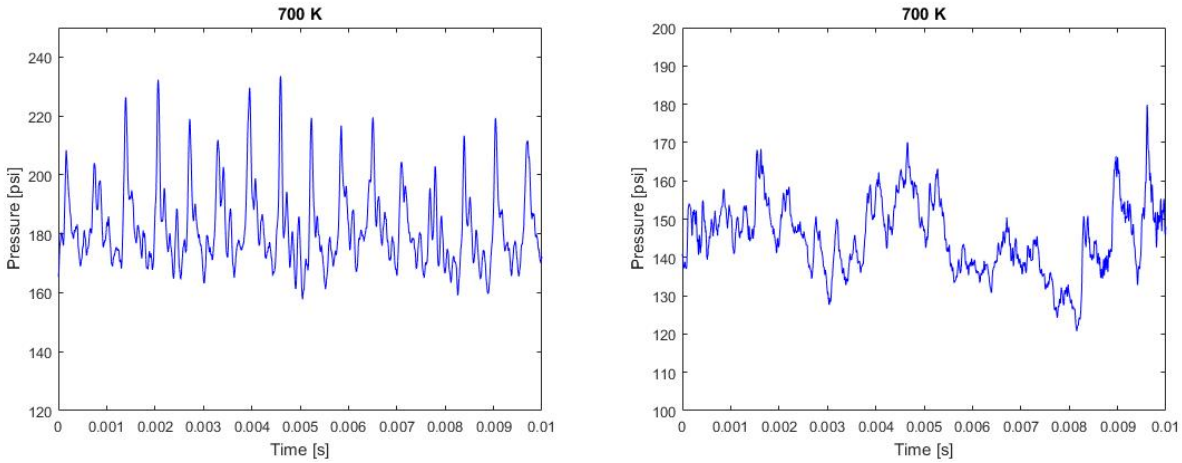

Fig. 8 Comparison of the pressure waveforms from the experiment at 700 K (L), and CFD simulation at 700 K (R). The pressure measurement is located at 0.3" downstream of the dump plane of the combustor.

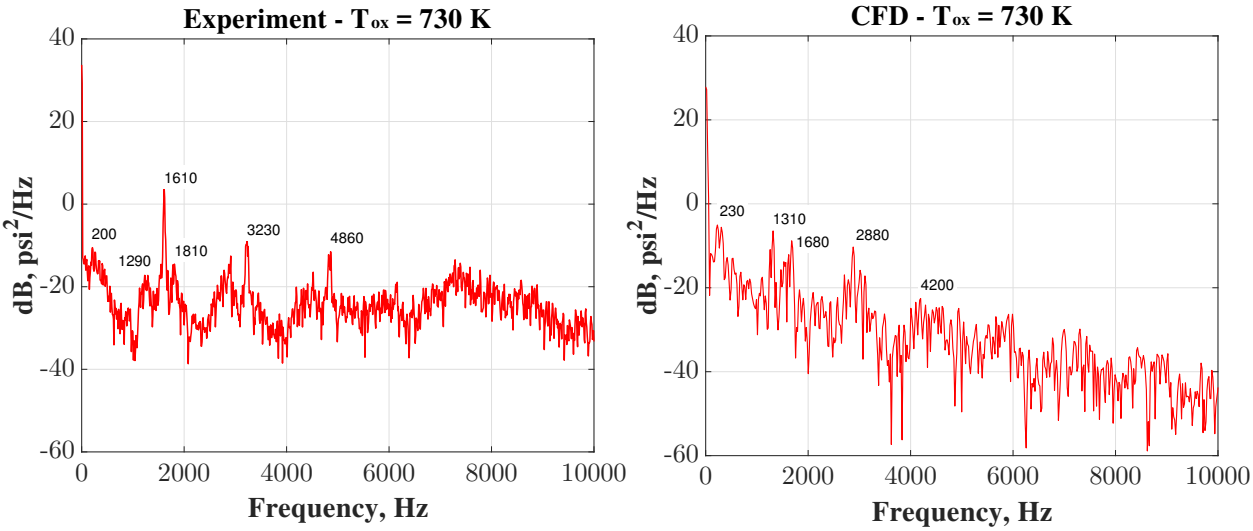

Fig. 9 Comparison of the pressure power spectral density from the experiment at 730 K (L), and CFD simulation at 730 K (R). The pressure measurement is located at 0.3" downstream of the dump plane of the combustor.

Experimental Results

Summary of Tests to Date

The main test variable to date has been oxidizer temperature. Before moving on to detailed results, it is useful to first show some general effects. Figure 11 shows measured c* and c* efficiency as a function of oxidizer temperature, and Figure 10 shows oxidizer velocity and momentum flux ratio as a function of oxidizer temperature.

The combustion dynamics, as expected, are highly dependent on how well the system is acoustically tuned. Acoustic tuning of the system can be achieved in two simple ways: changing the acoustic length or changing the sound speed. By changing the oxidizer temperature, the sound speed of the oxidizer in the oxidizer post is changed, but the density of the flow changes too, and in turn changes the injection velocity. Figure 11 (L) shows how the oxidizer velocity changes with oxidizer temperature. The injection mechanics can be characterized with momentum flux ratio, defined by the momentum flux of the oxidizer over the momentum flux of the fuel. For various flowing conditions Figure 11 (R) shows the relationship of the momentum flux ratio to the oxidizer temperature.

Figure 11 shows a proportional relationship between combustion performance with oxidizer temperature up until an

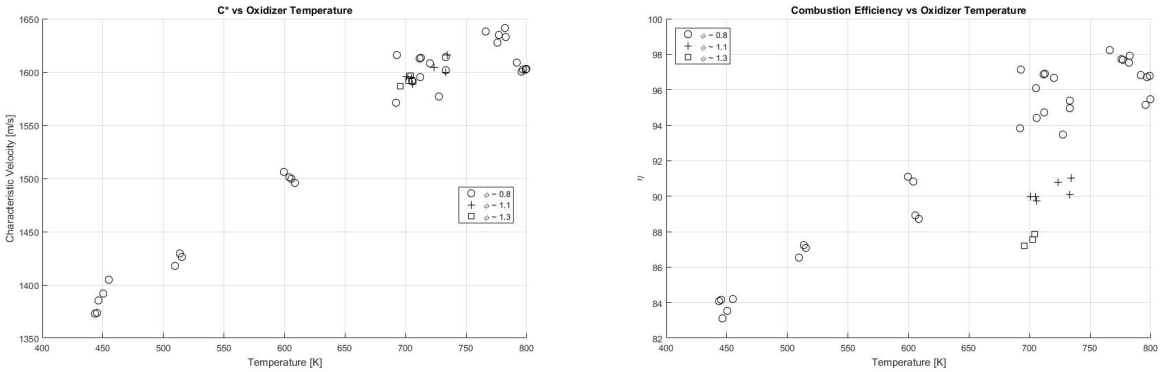

Fig. 10 (L) c* of HAMSTER as a function of oxidizer temperature, (R) combustion efficiency of HAMSTER as a function of oxidizer temperature

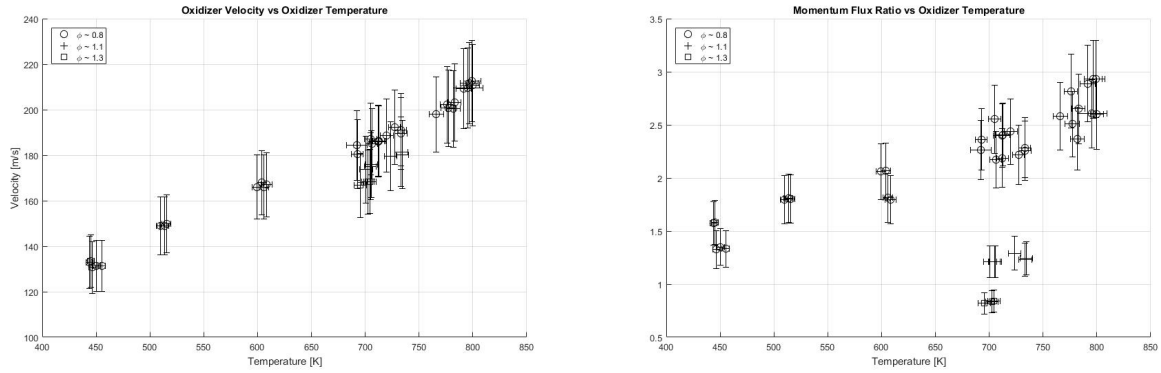

Fig. 11 Correlation of oxidizer velocity with respect to oxidizer temperature (L), and momentum flux ratio with respect to oxidizer temperature (R) for the current injector configuration

oxidizer temperature of $\approx 775K$, above which the combustion performance then decreases. Furthermore, it is interesting to note that c* appears to correlate more with oxidizer velocity rather than equivalence ratio, suggesting the dominating effect of oxidizer velocity on combustion efficiency. The increase in efficiency may also arise from stronger pressure fluctuations giving rise to better mixing; this is a fairly well known phenomenon. A major result was the observed coupling between the chug and acoustic instabilities, and the effect of oxidizer temperature on the coupling. At reduced oxidizer temperatures, which had poorer combustion efficiency, tended to have a more pronounced chugging mode, whereas thermoacoustic instability dominated at high oxidizer temperature. Figure 12 shows how the amplitude of each mode type varied with oxidizer temperature. Figure 13 also showed that when the chugging mode was significant the frequency at which it oscillated at appeared to be somewhat insensitive to the change in oxidizer temperature.

It should also be mentioned that each phenomenon was always present. Figure 13 shows how the frequency of each mode also varied with oxidizer temperature, and the change in the strength of the 1L thermoacoustic mode is shown in Figure 14. It is evident that the fundamental mode frequency (chamber sound speed) and the combustion efficiency are linked, as one would expect, and that these behaviors are inherently linked to the oxidizer temperature. It should be noted the oxidizer temperature also plays a major role in the ignition delay of methane; these effects may account for the relative change in combustion performance related to the change in equivalence ratio.

Mode Analysis

From the series of data a chugging mode appears to modulate the fundamental acoustic mode. From all the tests conducted a cross-correlation analysis of the measured pressure signals (Figure 15) shows a phase relationship or mode shape which indicates a bulk response in the chamber.

Cold flow tests at nominal test pressure were conducted, and bulk mode frequencies similar to those experienced

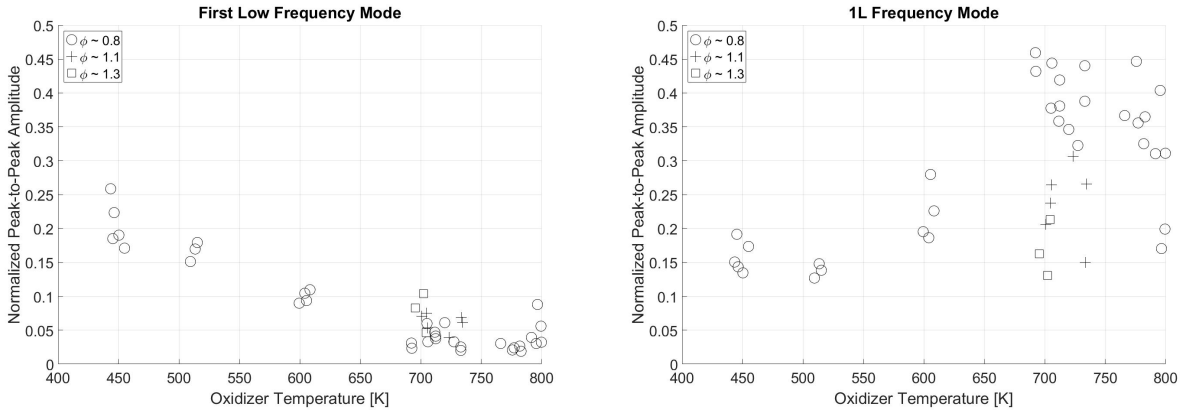

Fig. 12 (L) Chugging mode oscillation amplitude and (R) fundamental acoustic mode oscillation amplitude of HAMSTER as a function of oxidizer temperature.

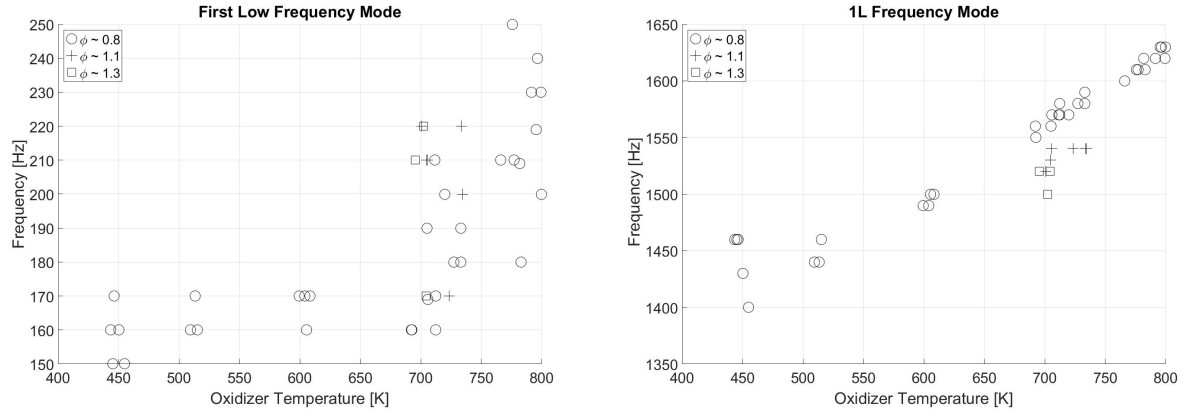

Fig. 13 (L) Chugging mode frequency and (R) fundamental acoustic mode frequency of HAMSTER as a function of oxidizer temperature.

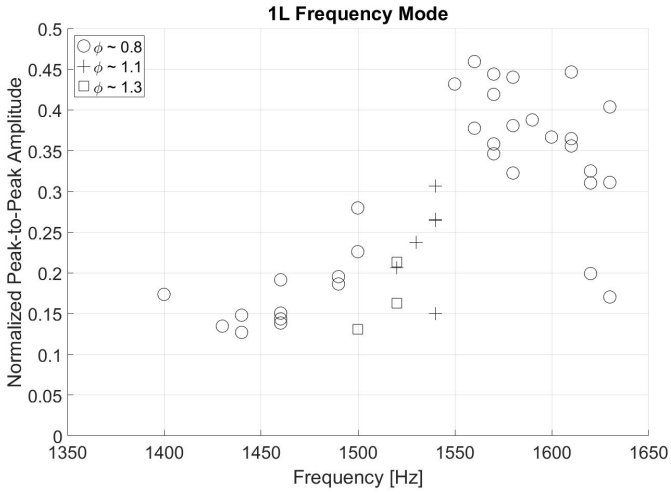

Fig. 14 Fundamental mode oscillation strength as a function of frequency.

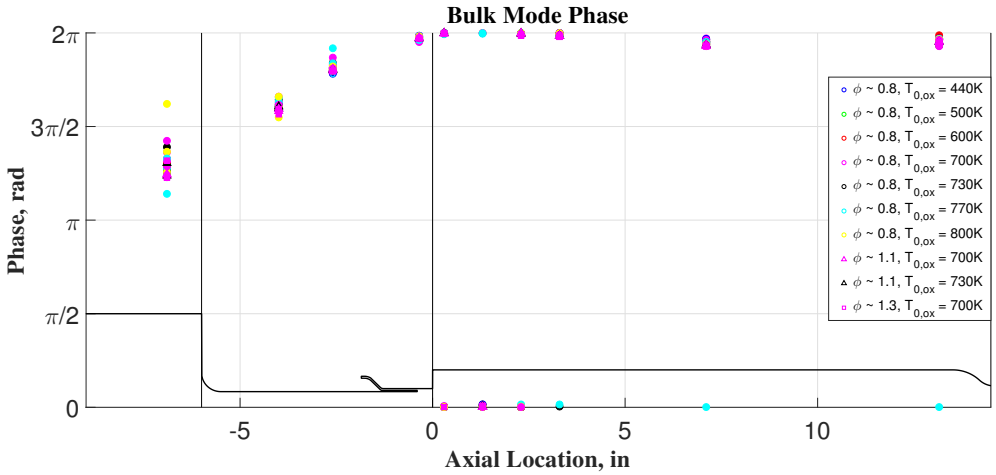

Fig. 15 Phase angle at the different pressure transducers for the chugging mode of every test.

during combustion were measured. Figure 16 shows that the bulk system response decreases in frequency with oxidizer temperature, and effectively shows that the chugging mode originates with the flow of the oxidizer. Synchronous combustion amplifies the oscillations.

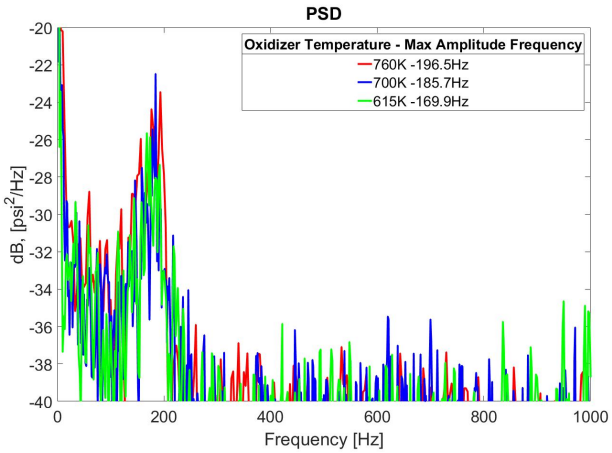

Fig. 16 System response at different oxidizer temperatures with the same mass flow rate.

A bicoherence analysis can be used to determine whether two signals are coupled, and was applied to the low frequency chug and higher-frequency acoustic mode instabilities. At 600K, both types of instability had relatively equal strengths, and this test case is used to illustrate how the modes are coupled. Figure 17 show the bicoherence plot along with the corresponding PSD over the same time window.

The points of intersection on the bispectrum plot represent a strong correlation between different frequencies within the time series of the signal. Since this is a third order moment, the plot cannot be used as a standalone tool and needs a corresponding second order moment correlation (PSD, FFT, etc.). The vertical and horizontal lines are correlations between a frequency and itself (autocorrelation) and its harmonics. The diagonal lines represent a cross-frequency correlation, which means that one or more frequencies are modulating another frequency. This plot doesn't describe how the modulation occurs, only that there is one, and what type of modulation. From the PSD in Figure 17, upon looking at the fundamental mode at $\approx 1500Hz$, there appears to be frequencies associated with resulting modulated frequencies (green) corresponding to the the fundamental mode (carrier frequency) modulated by the chugging mode $\approx 170Hz$ (modulating frequency). The appearance of satellite peaks on the PSD, separated from the main peak by a frequency close to the chug frequency, was a common occurrence and will be analyzed further here with a wavelet analysis and later using results from high-fidelity simulations of the experiment. The satellite peaks will be defined as L- or L+.

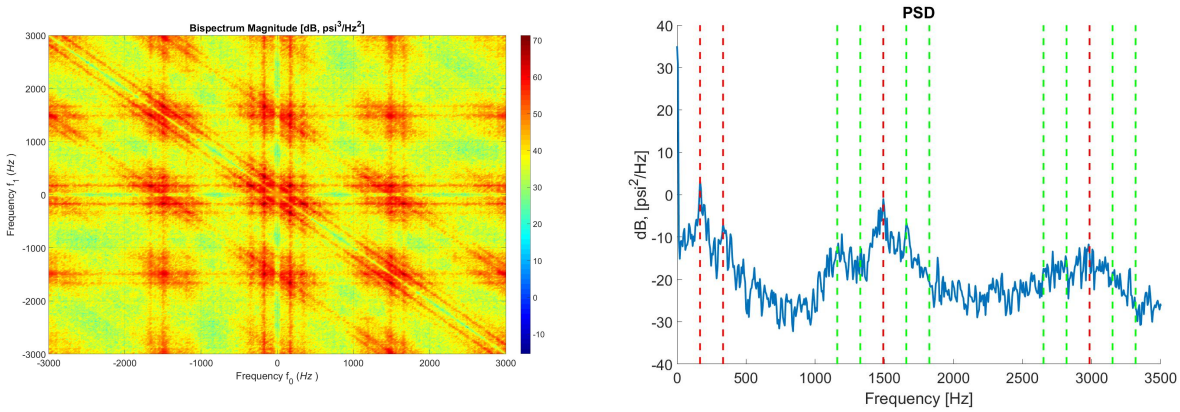

Fig. 17 (L) Bispectrum plot and (R) PSD of a test with 600K oxidizer temperature. The red lines on the PSD correspond to the main physical modes and the corresponding harmonics (overtones).

A wavelet analysis of the same test, during the same time window, is shown in Figure 18. It is apparent that the fundamental mode is in fact frequency-modulated in time with a period corresponding to the chugging frequency. To illustrate the periodicity of the frequency modulation better, a wavelet transform of a test with a more pronounced thermoacoustic mode is shown in Figure 19; this test corresponds to a oxidizer temperature of $760K$. The periodic increase and decrease in frequency corresponds to the chugging frequency and the periodicity of the intermittent power fluctuation corresponds to the harmonic of the chugging frequency. The frequency relationship behind this sort of behavior is revealed in the bispectrum plot whereby there is a correlation between the chugging mode, its harmonic, the thermoacoustic mode and its corresponding modulated frequencies.

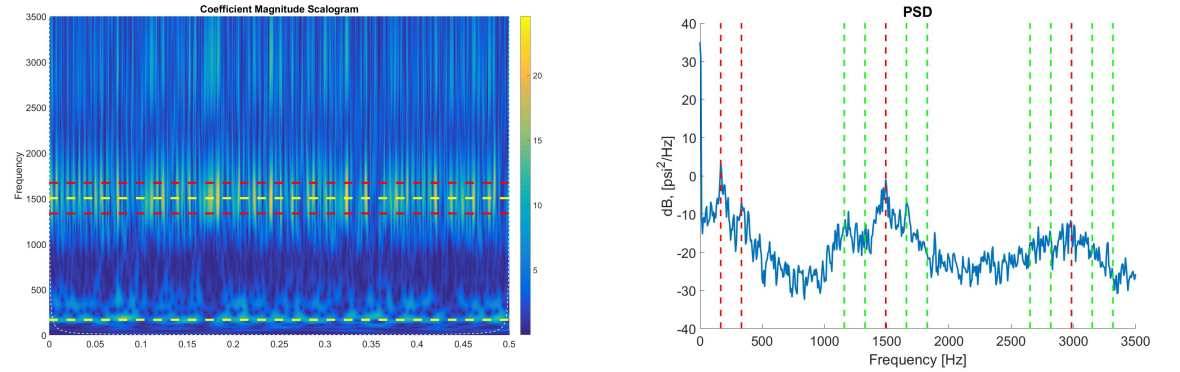

Fig. 18 (L) Wavelet coefficient scalogram plot and (R) PSD of a test with 600K oxidizer temperature. The yellow lines on the wavelet plot correspond to the main physical modes, while the red lines outline the frequency band through which the fundamental mode oscillates in time. The red lines on the PSD correspond to the main physical modes and the corresponding harmonics (overtones).

Chemiluminescence Analysis

In conjunction with the pressure measurements, high frequency (> 250 kHz) measurements of the chemiluminescent emissions from the injector recess and chamber are obtained at several spatial locations. Chemiluminescence emissions measurements typically target the line of sight apparent flame location. The flame location and its dynamics in this particular case are more challenging due to the shear co-axial injection at relatively high pressure drops. The resulting flame zones correspond to the fluctuating shear layer, recirculating flow in the corner of the head end of the combustor and the wall interactions of the injected fuel. An important purpose of measuring chemiluminescence in the present study is to track several of these phenomena and their comparison with the predictions of the simulation. Thus

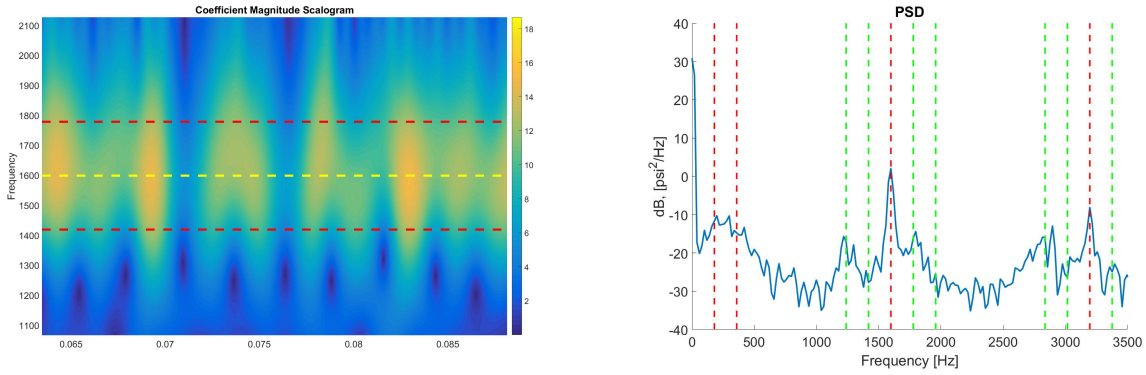

Fig. 19 (L) Wavelet coefficient scalogram plot and (R) PSD of a test with 760K oxidizer temperature. The yellow line on the wavelet plot corresponds to the unaltered 1L mode of the chamber, while the red lines outline the frequency band through which this mode oscillates in time. The red lines on the PSD correspond to the unaltered acoustic modes and corresponding harmonics (overtones), and the green lines indicate the frequency modulation of the acoustic modes that are separated from the main modes by a frequency equal to the chug modes.

validated simulation can provide significant insight into the coupling of the heat release events to the fluid dynamic phenomena under high pressure, non-premixed conditions. The design of the hardware facilitating the high frequency chemiluminescence measurements is shown in Figure 20.

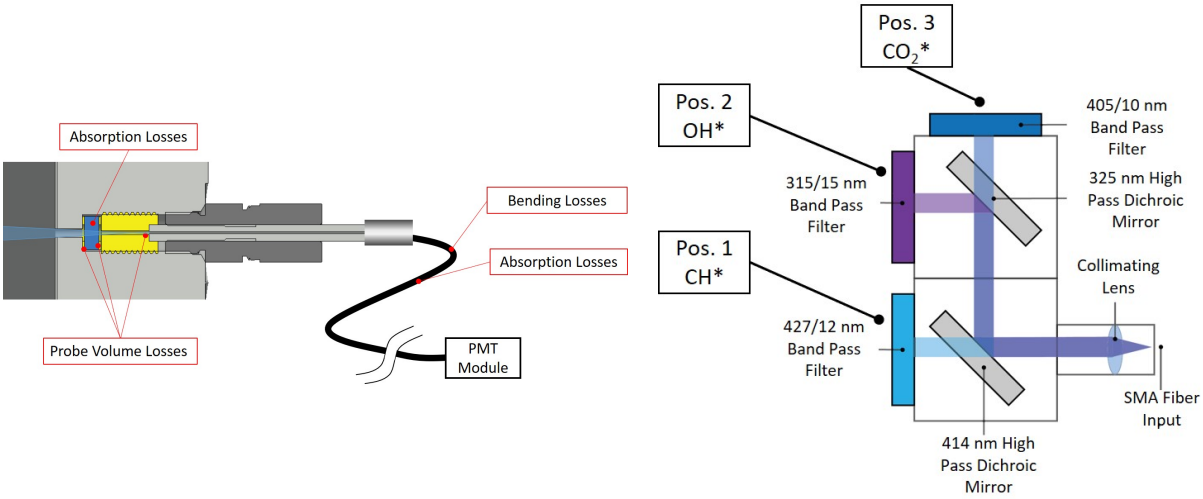

Fig. 20 (L) PMT fiber optically coupled port design with expected losses and (R) the optomechanical setup to filter and extract the relevant portions of the spectral radiation.

Typically the frequency content of the PMT signals resembles the frequency content of the pressure signal. Figure 21 shows how the OH* emission signal in the injector recess fluctuates at the same frequencies as the pressure signal. It is interesting that the emission signal correlates well with the pressure signal, but more interestingly is the presence of frequencies in both signals which do not correspond to acoustic harmonics of the primary oscillation. The spectral range of interest, though, is in the region of 7500-12000 Hz corresponds to the vortex shedding frequency from the fuel collar [6]. Evidence of this, but still yet to be confirmed, is in the OH* spectrum, one value at $\approx 10050Hz$ and another at $\approx 11500Hz$. Further examination of Figure 21 accentuates the troughs in the PSD of the pressure signal. The troughs are indicative of antiresonance in the system, which may be as important as the resonance.

The PMT probe chord locations tend to show a similar agreement with the pressure signal, except for the chord location on the outer most edge of the chamber, nearest to the head end, where no signal is most often detected. This is

indicative of a lack of combustion in the recirculation zone. In some cases, where there was a strong chugging mode, there was a weak signal detected.

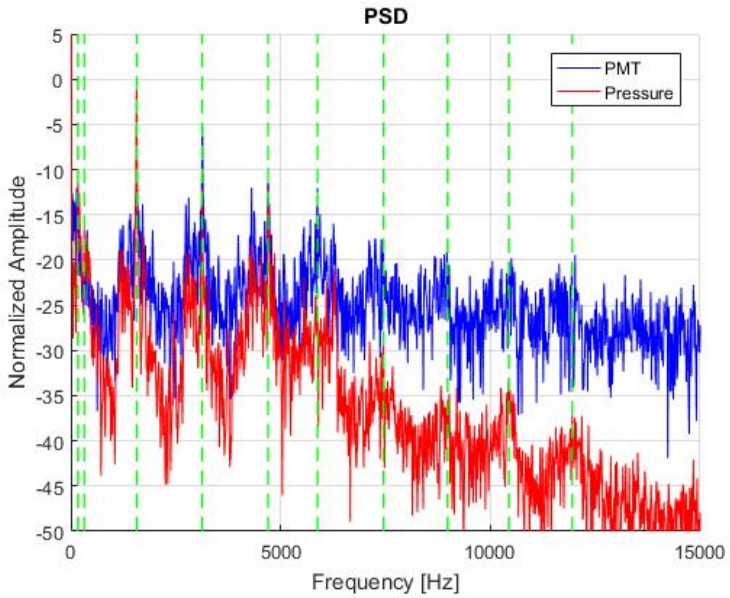

Fig. 21 OH* chemiluminescence and pressure PSDs at -0.35" from the dump plane of the combustor, for a test with oxidizer temperature of 700K. The green lines highlight some frequencies that are correlated; the frequencies in sequence are (170, 320, 1570, 3130, 4700, 5880, 7450, 9000, 10440, 11950) Hz.

By taking the cross-correlation between the signals at the -0.350" location (just downstream of the fuel collar) and the 0.300" chord location, at the outermost edge of the chamber cross-section, of the CH* signal, and then averaging the spectra for all the tests, Figure 22 suggests that one of the primary frequencies associated with the fluctuating combustion dynamics appears to be around 7200Hz, regardless of oxidizer temperature.

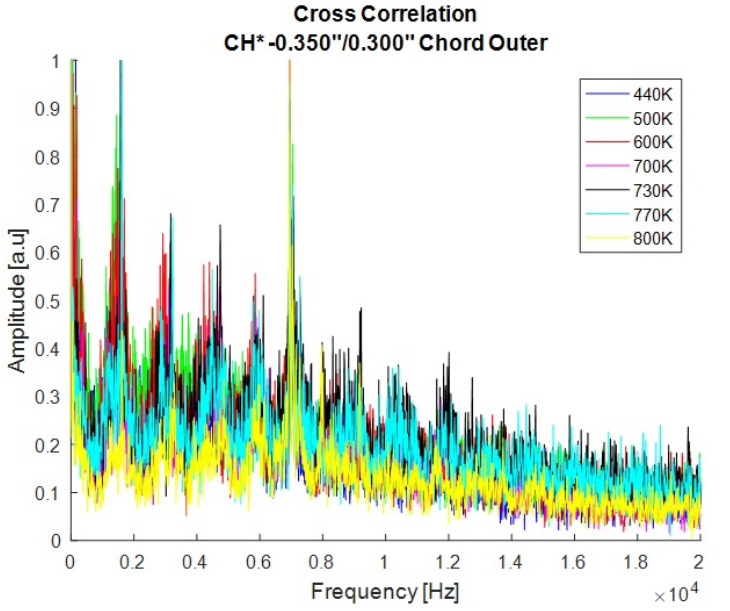

Fig. 22 Averaged cross-spectra across all tests for the -0.350"/0.300" chord outer locations.

Whereas pressure data can be easily compared, PMT measurements cannot be directly compared to the simulation

outputs. To reconcile the different forms of data related to the chemiluminescent radiative output, a model was developed to produce radiative output for comparison to the data collected from the PMT probes. Since the CFD domain is axisymmetric along the mean flow path and the PMT probe volumes are orthogonal to the line of axisymmetry, it was necessary to construct a 3D domain from the CFD grid and then extract the relevant data within each probe volume domain intersecting with the newly constructed 3D domain. To construct the new 3D domain, each 2D axisymmetric element was segmented into 3600 new equiangular cells, and each new cell would adopt the information from the original cell. Then using a ray tracing algorithm (Figure 23), based on the port design and geometry of the optics associated with the fiber optic probe, the spatial domain of the probe volume was determined. Then only the cells from the new 3D domain that fell within the probe volume domain would contribute to the emissions expected to reach the PMTs.

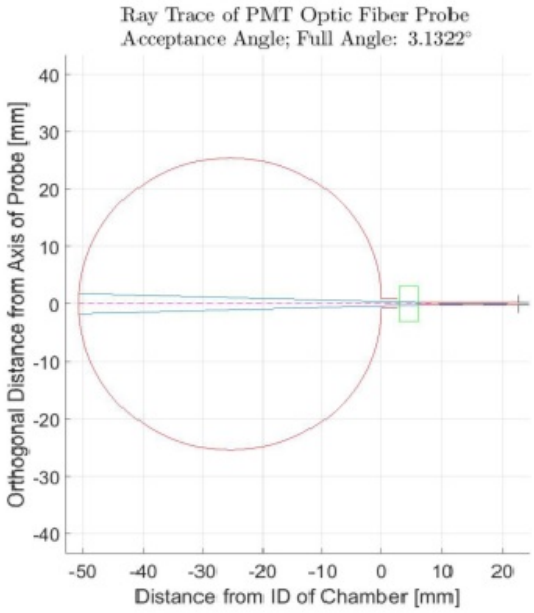

Fig. 23 Probe volume domain determined by a ray tracing algorithm incorporating the geometric aspects of the port and numerical aperture of the fiber optic probe. The chamber inner diameter is drawn in red, while the rays at the extremity of the probe volume domain are drawn in blue.

Using the location of each of the cells relative to the aperture of the port, the radiative flux reaching the port from each cell location was determined. The relative radiative flux was based on the assumption that each cell emitted in all directions evenly. The possible fraction of light entering the port is thus based on the solid angle subtended by the port aperture as a fraction of 4π steradians. The solid angle fraction for a typical probe volume cutting across the diameter of the chamber is shown in Figure 24.

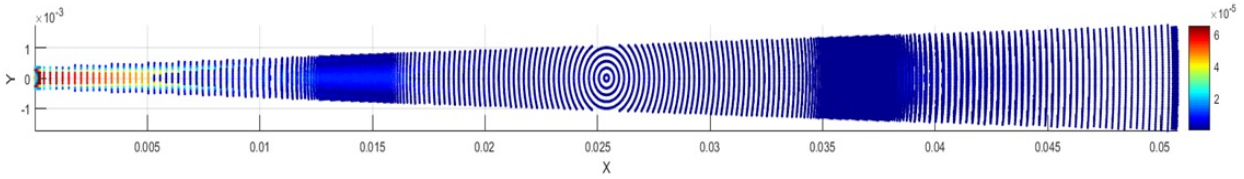

Fig. 24 Fraction of light entering the port aperture for each point emitter in the probe volume.

The number of photons emitted in the spectral range based on OH* and CH* was calculated using the density, volume and mass fractions of the excited species for each cell, and the number of photons reaching the PMT was corrected using the solid angle fraction for each cell. Figure 24 shows that the radiative contribution from emitters close to the aperture are an order of magnitude greater than those located on the opposite side of the combustor.

Figures 25 and 26 compare pressure and chemiluminescence from measurement and prediction over the interval of a chug cycle. The data were normalized using maximum and minimum values within the time frame selected. In general the CH* emission power is at least an order of magnitude lower than that produced by OH* for both experiment and simulation. In both datasets, for both experiment and simulation, the signals from CH*, OH* and pressure do not correspond in phase. These comparisons provide an extra level of validation and allow detailed study of how the reacting flow evolves.

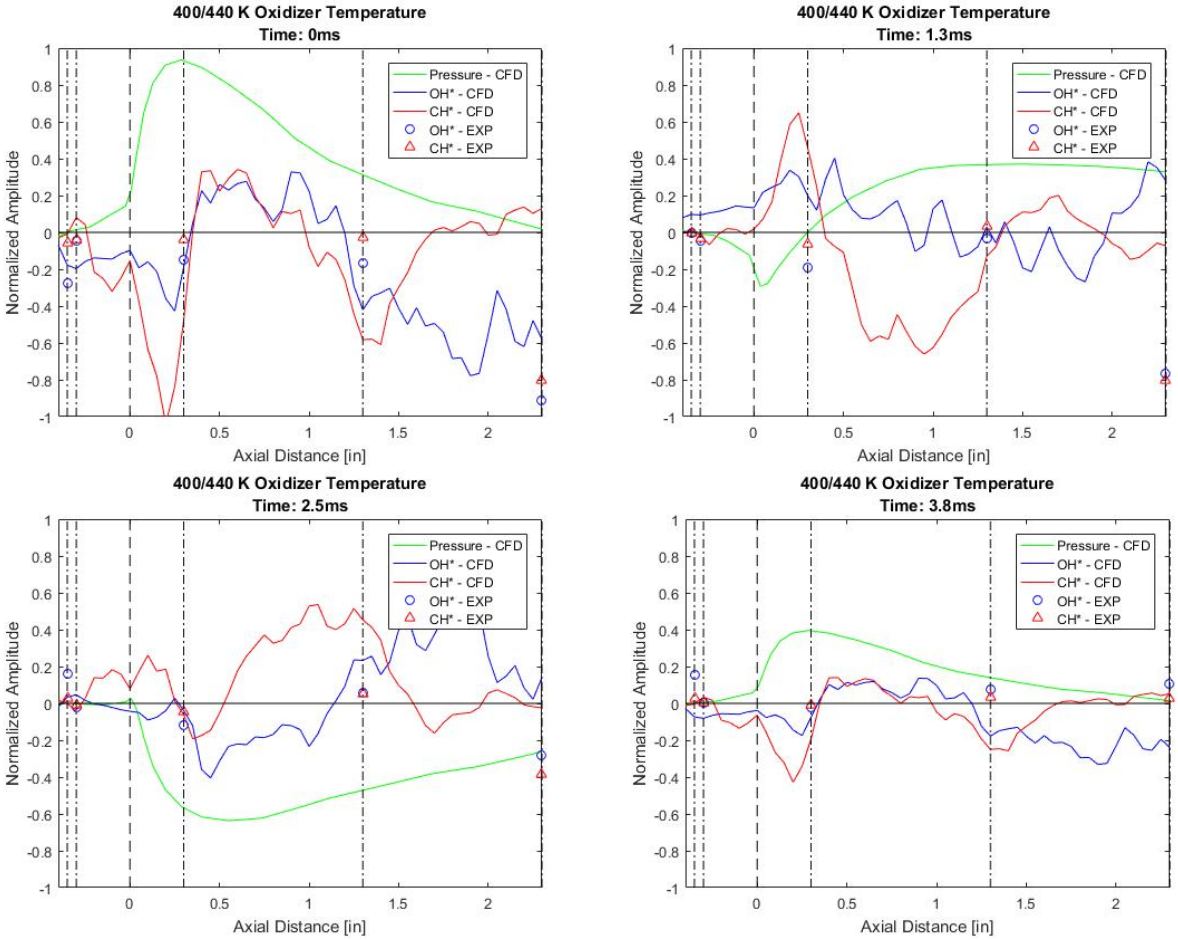

Fig. 25 Comparison of chemiluminescent data from the CFD simulation involving an oxidizer temperature of 400K and the experiment with an oxidizer temperature of 440K.

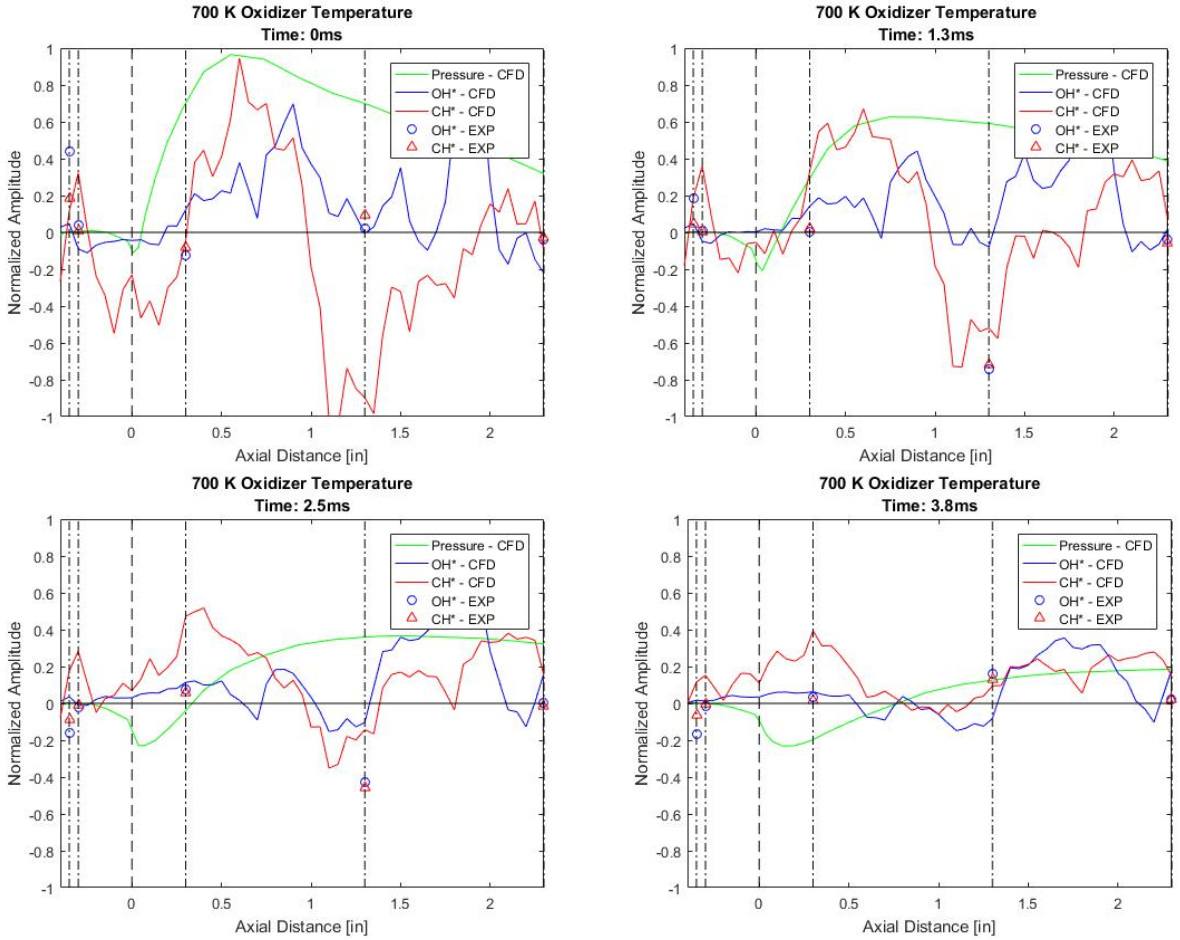

Fig. 26 Comparison of chemiluminescent data from the CFD simulation and the experiment with an oxidizer temperature of 700K.

Detailed Study of Computational Results

The study described here uses concurrent simulation, analysis and measurement of the self-excited combustion instabilities that are dependent on flow and geometric parameters. Experimental observations measured over a broad range of test conditions motivate a more detailed study of key physics. In the following sections, results from high fidelity simulations of the study configuration are used to provide further detail on the combustion dynamics.

Simulation Results

Two computational cases are presented here with oxidizer temperatures of $T_{ox} = 400\ K$ and $T_{ox} = 730\ K$. Both cases operate with an equivalence ratio $\phi = 0.8$ and the same mass flow rate and operating conditions detailed in Table 1. The fuel inlet uses a choked inlet, which is consistent with the experiments.

Figure 27 depicts the spectra obtained from Dynamic Mode Decomposition (DMD) analysis of the pressure and heat release fields, showing the most dominant modes of each. Although the temperature is lower than the 440 K case, the comparison of the simulation DMD pressure mode frequencies with the PSD of the experimental results in Fig. 7 shows a good agreement. In both the experiment and the simulation, at lower oxidizer temperature the low frequency instability is predominant, whereas its intensity decays with increasing oxidizer temperature. As shown in Figure 7, in the experiment at $T_{ox} = 440K$, there is a dominant chugging mode at 160 Hz, and a lower power 1L mode at 1460 Hz (170 and 1450 Hz, respectively in the simulation). In contrast, for the experiment at $T_{ox} = 730K$, the 1L mode at 1610 Hz dominates the spectra and the chug mode has a lower amplitude at 200 Hz (Figure 9). In both oxidizer temperature cases, it is also noteworthy the presence of two modes at lower and higher frequency around the 1L mode,

henceforth referred to as $1L^-$ and $1L^+$. For the case at $T_{ox} = 730K$, the simulations capture the decreasing trend of chugging intensity but overestimate it with respect to the experiment. In addition, in the simulations the $1L^-$ mode replaces the 1L observed in the experiment as well as the fact that the $1L^+$ appears to be of lower magnitude.

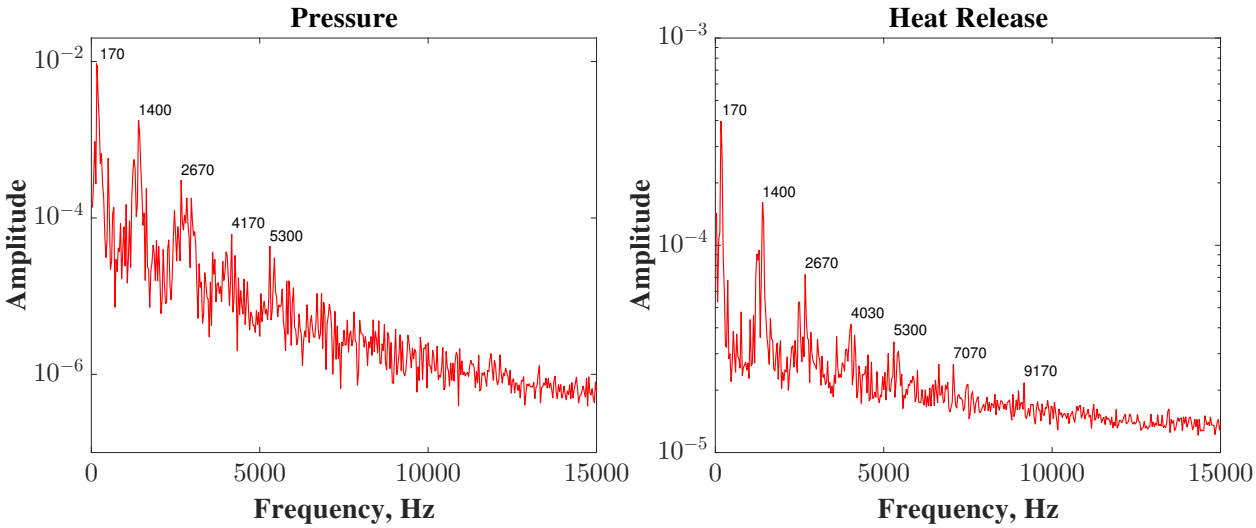

Fig. 27 Dynamic mode decomposition spectra of the pressure and heat release for the case $T_{ox} = 400\ K$. The $1L$ acoustic mode at $1400\ Hz$ has two adjacent longitudinal modes referred to as $1L^-$ and $1L^+$ at $1270\ Hz$ and $1630\ Hz$, respectively. In the heat release plot, the high frequency modes at $7070\ Hz$ and $9170\ Hz$ do not match with multiples of the acoustic modes harmonics suggesting that they may be related to hydrodynamics or chemical kinetics.

In the simulations and experiments the $1L^-$ and $1L^+$ have a mode shape very similar to a typical 1st longitudinal chamber mode (Figure 28). In the experiments, the frequency difference between the 1L mode and the adjacent $1L^+$ corresponds to the chug mode frequency. In both cases, the $1L^+$ mode occurs at a frequency of $f_{1L^+} = f_{1L} + f_{chug}$. The relation of the frequency of the $1L$ and $1L^+$ suggests that the latter mode is related to the chug mode, and proof of this was presented above. Since the chug period is much longer than the 1L mode, as the bulk pressure changes very slowly when compared to the former, the 1L mode effectively sees a higher or lower chamber pressure and different mean flow properties depending on the relative position in the chug cycle. The change in chamber pressure may affect the dynamics of the 1L mode differently during different parts of the chug cycle. The variation of the 1L mode during the chug mode cycle, with oscillatory changes in the mean speed of sound of the chamber, provokes the modulation of its acoustic frequency following the chug mode oscillations. The spectrum of a signal modulated with frequency modulation features adjacent peaks surrounding the carrier signal frequency separated by multiples of the modulation signal frequency. Using the analogy of frequency modulation of a signal in this case, the carrier frequency would be the 1L acoustic mode, which would be frequency modulated by the chug mode oscillations. Both the PSD and DMD spectrum of such a frequency-modulated signal would feature a strong 1L mode frequency with adjacent peaks at a frequency difference corresponding to the chug mode frequency. It should be noted that the time evolution of the flow field in a realistic combustor such as the present configuration can be highly variable due to the high level of unsteadiness. Therefore, in this case the frequency modulation would not necessarily be symmetric between the $1L^-$ and $1L^+$ frequencies.

The high-fidelity simulations presented in this section also predict this behavior of the 1L mode with its adjacent modes. In the simulations, although the frequencies of the modes are very close to the experimental results, the frequency difference between the $1L$ and $1L^+$ mode is not as consistent. It should be pointed out that the sampling interval for the CFD simulation is limited compared to the experiment due to computational time constraints. in Figure 27, the heat release modes correspond to the low frequency mode (170 Hz) and harmonics of the 1L up until the 4th longitudinal acoustic mode. The higher frequency modes at 7070 Hz and 9170 Hz are not multiples of the fundamental acoustic mode. They may be related to natural hydrodynamic modes initiated in the reacting shear layer behind the collar that separates the fuel and oxidizer, and at the exit of the injector tube at the inlet to the combustion chamber. Figure 28 shows the DMD mode shapes for the chugging mode and the 1L mode for $T_{ox} = 400\ K$. The low frequency

mode clearly matches the measured mode shown in Fig. 15 as the chamber shows no spatial variation in the pressure mode. The 1L mode in Fig. 28 also follows the expected behavior and is confirmed by the mode shape of the pressure transducers.

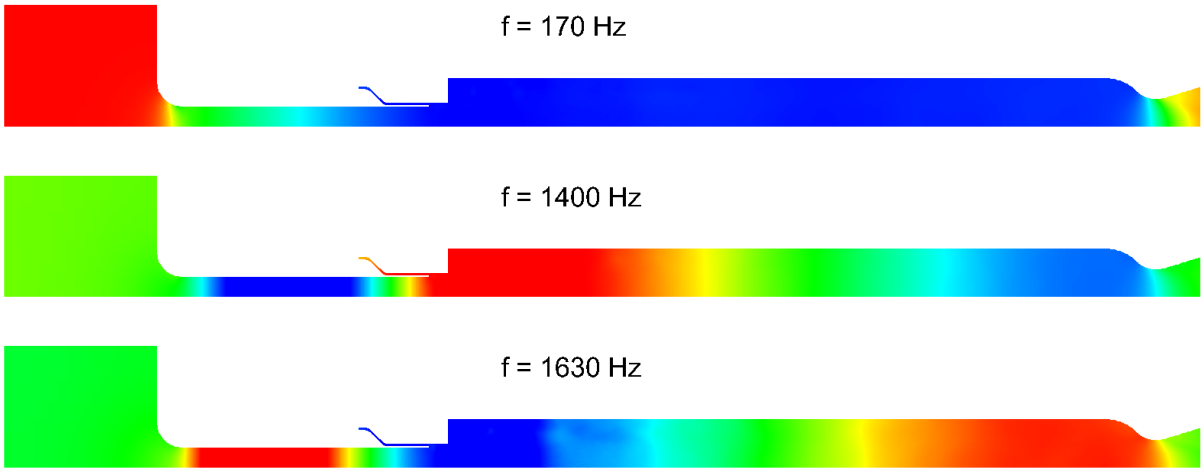

Fig. 28 Dynamic mode shapes of pressure for the case $T_{ox} = 400\ K$. From top to bottom the modes represent the chugging mode, $1L$ and $1L^{+}$ mode, respectively. The color scale is not shown because it does not represent magnitude.

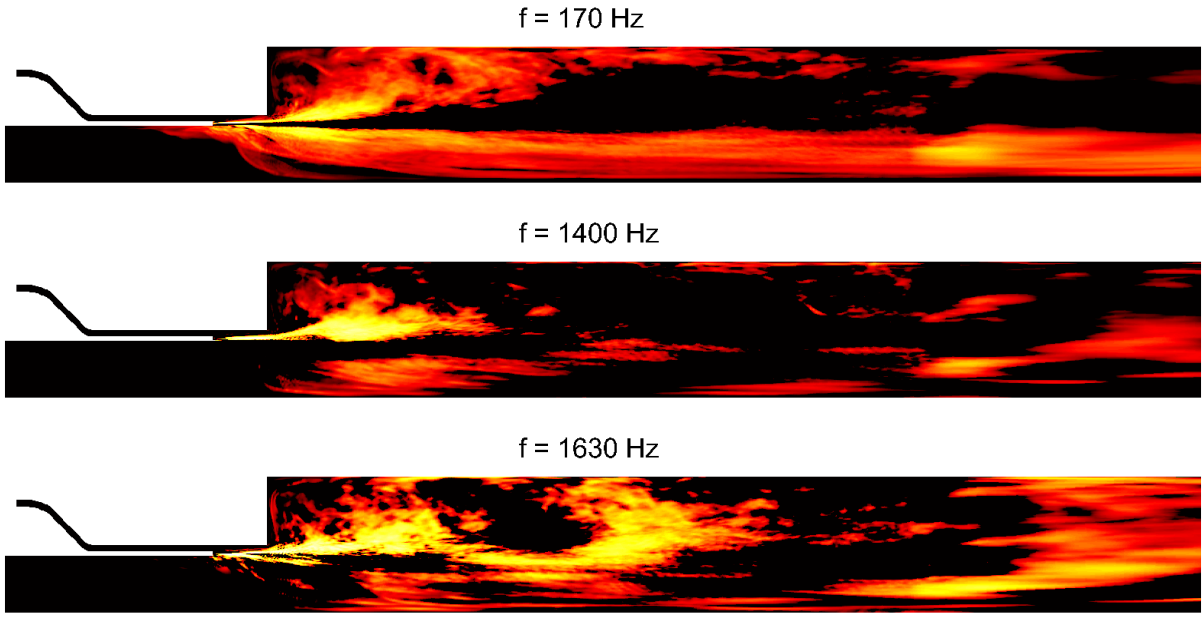

Fig. 29 Dynamic mode shapes of heat release for the case $T_{ox} = 400\ K$. From top to bottom the modes represent the chugging mode, $1L$ and $1L^{+}$ mode, respectively. The color scale, which is exponential, is not shown because it does not represent magnitude.

Chug cycle analysis

Figure 29 shows the DMD mode shapes of heat release for the case $T_{ox} = 400\ K$. For the chug mode at 170 Hz, there is a heat release combustion response except in the shear layer. One of the major areas of this response is in the recirculation zone. The heat release mode propagates from the edge of the fuel collar all the way to the end of the recirculation zone. The analysis of the chug cycle shown in Figure 30 further illustrates how the chugging mode is related to the dynamics of the recirculation zone. In this case, the chugging instability is dominant provoking large variations of the ox post flow velocity and mass flow rate across the injector, so that the vortex shedding dynamics downstream of the dump plane may vary significantly during the chug mode cycle. In turn, these fluctuations in the vortex shedding dynamics may affect the mixing process of the fuel and oxidizer with the consequent fluctuations in heat release. On the other hand, the 1L mode shows a strong heat release response in a small area close to the dump plane and below the recirculation area. The heat release contours of Fig. 30 show this as approximately the first large scale vortex shed off of the dump plane.

Figure 30 shows a typical cycle during the low-frequency chug mode for the case $T_{ox} = 400\ K$. Chug instabilities are in general related to mass flow fluctuations and are characterized by low frequencies and no spatial dependence of the pressure across the chamber. At the start of the cycle, the pressure at the dump plane is at its low point of the cycle. A large pressure difference therefore exists between the oxidizer manifold and the dump plane of the combustor, increasing the oxidizer mass flow. The axial velocity in the oxidizer post shows acceleration, which sustains the oxidizer jet for a greater length inside the combustor. In this portion of the cycle the higher oxidizer flow velocity appears to promote finer mixing with smaller scale vortices that appear less perturbed by the reciculation zone than at the peak of the cycle. The resulting heat release contour is shown in plots A) and B) of Fig. 30. As the oxidizer flow accelerates and the mass flow rate entering the chamber increases, the pressure starts to build up thereby slowing the increase in oxidizer mass flow rate due to the pressure differential with the oxidizer manifold decreases. At the peak of the cycle C), with the pressure of the dump plane reaching its highest value, the mass flow rate entering the chamber starts to decrease thereby inducing a decrease in chamber pressure. This decrease in mass flow rate entering the chamber effectively leads to a deceleration of the ox post flow velocity so that the oxidizer jet penetrates less into the chamber. Moreover, in the descending phase of the cycle D), the lower oxidizer velocity appears to provoke a stronger interaction between the oxidizer jet and the recirculation zone downstream of the dump plane and features large scale vortical structures being shed downstream. This effect promotes more mixing of the fresh propellants with the hot gas at the recirculation zone with the consequent fluctuation in heat release which then contributes to the pressure build up for the next cycle.

The fluctuations in the fuel and oxidizer flow as they are influenced by the instability in the chamber are important since these contribute to the fluctuations in the local mixture ratios and thus the heat release characteristics of the combustor. The heat release is an extremely non-linear phenomena, which has several orders of magnitude fluctuations within the flame length scales, enabling coupling with various fluid dynamic scales. Figure 31 shows the PSD of the mass flow rate of oxidizer and fuel at the edge of the fuel collar (as shown in Figure 2). The comparison highlights that the oxidizer mass flow rate is strongly affected by the low frequency mode, whereas the fuel mass flow rate is driven primarily by the acoustic modes. Thus, the chug mode in this case is coupled with the oxidizer flow.

Figure 33 shows the evolution of the spatially-averaged chamber temperature over time compared to the pressure trace close to the dump plane. The spatially-averaged chamber temperature is a good representation of the fluctuation of the mean flow properties over time. The evolution of the chamber temperature is very smooth compared to the pressure trace due to the spatial-averaging, which cancels out the local fluctuations and thus reveals the overall trends. The chamber temperature clearly appears to follow the chug mode oscillations with a minor presence of the 1L mode fluctuations. In turn, the oscillations of the chamber temperature translate into the speed of sound, which then affects the frequencies of the acoustic modes. As the period of the chug mode is much longer than the 1L mode, the latter mode effectively experiences different mean flow properties depending on the relative position within the chug cycle. Thus, the fluctuation of the mean speed of sound of the chamber following the chug mode oscillations, provoke the modulation of 1L mode acoustic frequency.

The cycle analysis and heat release DMD modes suggested a connection between the chug mode and the recirculation zone dynamics. In [7] Culick modeled the recirculation zone with an approximation considering it as a chemical reactor whose behavior is known to be well-characterized by the temperature of the incoming gases entrained from the environment, and the average temperature within the zone. Figure 33 shows the results of this simplified calculation based on energy and mass flows considerations. In this analysis, the upper and lower branches of the hysteresis loop represent different branches of stable combustion. Work from Knoop [9] et al and Isella [10] et al, confirmed through high speed films that the upper branch of the loop is associated with shedding of large vortices which, causing periodic combustion of entrained reactants sustain high amplitude pressure oscillations. In contrast, the lower branch is associated

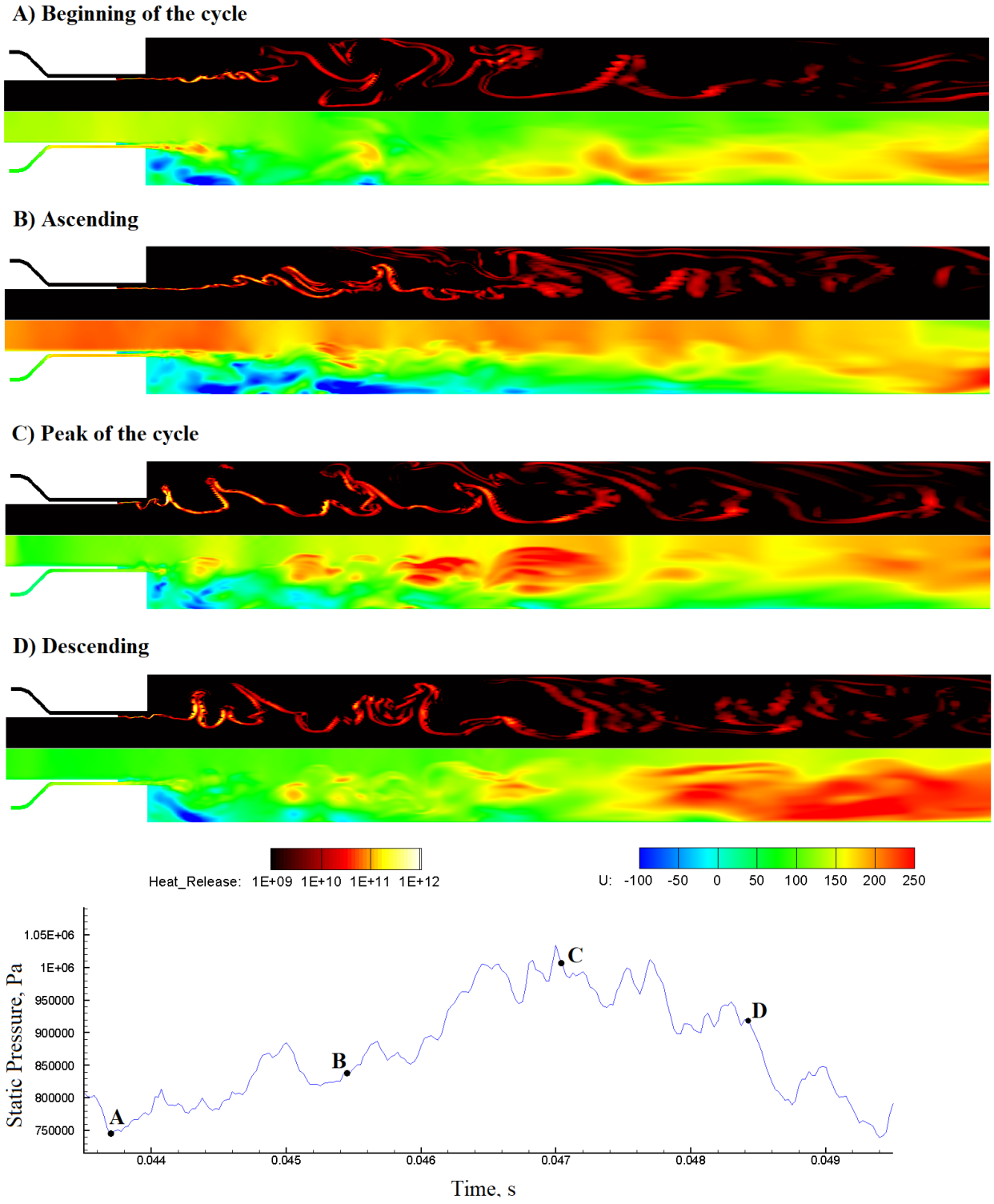

Fig. 30 Evolution of a typical chugging mode cycle for $T_{ox} = 400\ K$. The pressure trace is located at 0.3" downstream the dump plane. The contour plots show heat release in W/m^3 (top) and axial velocity in m/s (bottom). The color scale for the axial velocity has been deliberately limited to lower bounds in order to better appreciate the velocity fluctuations inside the ox post and chamber.

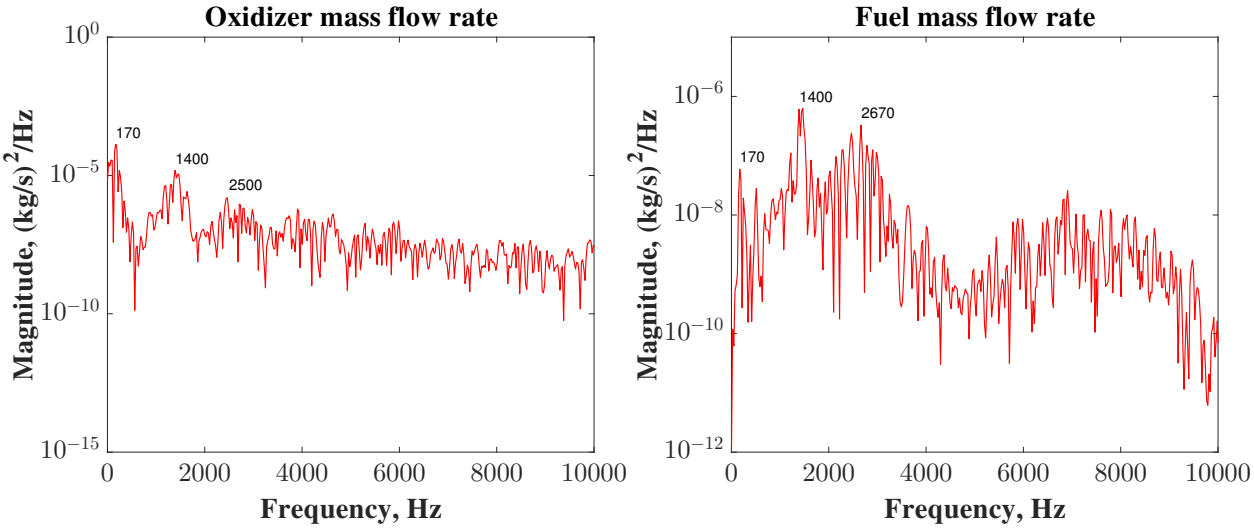

Fig. 31 Power spectral density of the oxidizer and fuel mass flow rate, respectively, for the case $T_{ox} = 400\ K$.

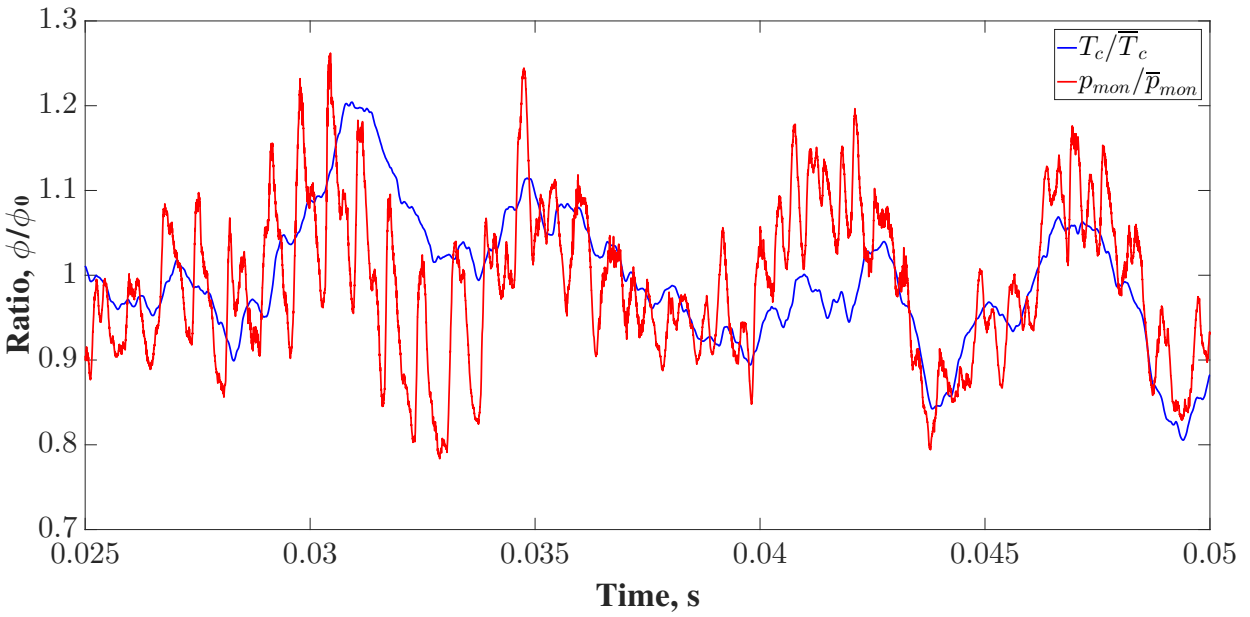

Fig. 32 Time evolution of the spatially-averaged chamber temperature and pressure trace at a monitor point located 0.3" downstream the dump plane for the case $T_{ox} = 400\ K$.

with relatively quiet combustion in a shear layer shed from the lip at the inlet [7]. Applied to the study configuration, faster oxidizer flows which penetrate deeper into the chamber and promote finer scale mixing with smaller vortices, are more representative of the lower branch which exhibits quieter combustion. Effectively, a finer scale and more efficient mixing process with smaller eddies generates a broader spectrum of oscillations that are less coherent, and hence, quieter. Conversely, for slower oxidizer flows the increased interaction with the recirculation zone with large scale vortical structures being shed off of the dump plane resembles more the upper branch. In this regime, the periodic entrainment of pockets of reactants into the recirculation zone, which eventually react strongly generating large pressure fluctuations, couples with the acoustic modes thereby closing the feedback loop that leads to stronger combustion instabilities.

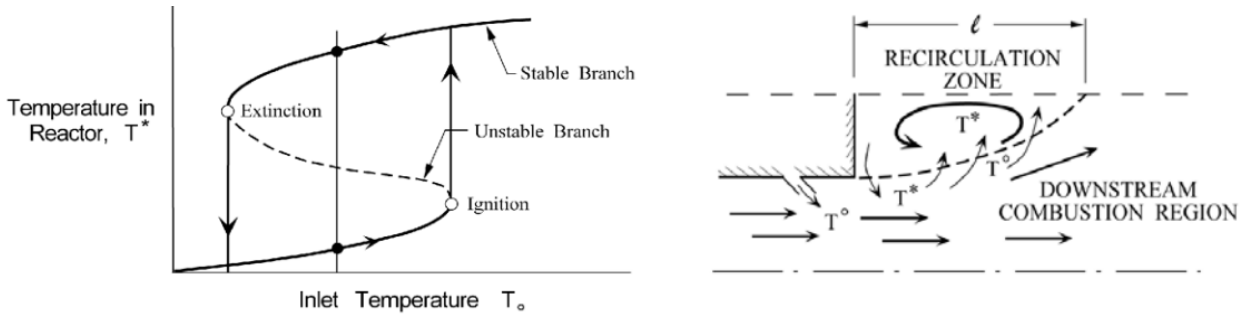

Fig. 33 L) Hysteresis loop for a recirculated zone idealized as a simple chemical reactor (from Culick [7]). R) Sketch of a recirculation zone formed by a jet of fuel or oxidizer (adapted from Natanzon [8]) in Culick [7]).

Analysis of the Reacting Shear Layer Ignition Dynamics

Time accurate simulations allow a more detailed examination of the reacting flow field through the use of heat release statistics. A scatter of the mean heat release and corresponding standard deviation at each discrete location in the simulation helps identify the important features of a flame such as the flame anchoring location. For the new experimental combustor, such a scatter at the two conditions of operation are shown in figure 34. Both plots show a sharp peak in the mean heat release at the beginning of the injector recess. Some of the heat release at the lower temperature is present at an upstream location. The likely reason for this is the behavior of the corner recirculation zone, which as described before, undergoes periodic re-ignition events corresponding to the coupled fluid-dynamic instability.

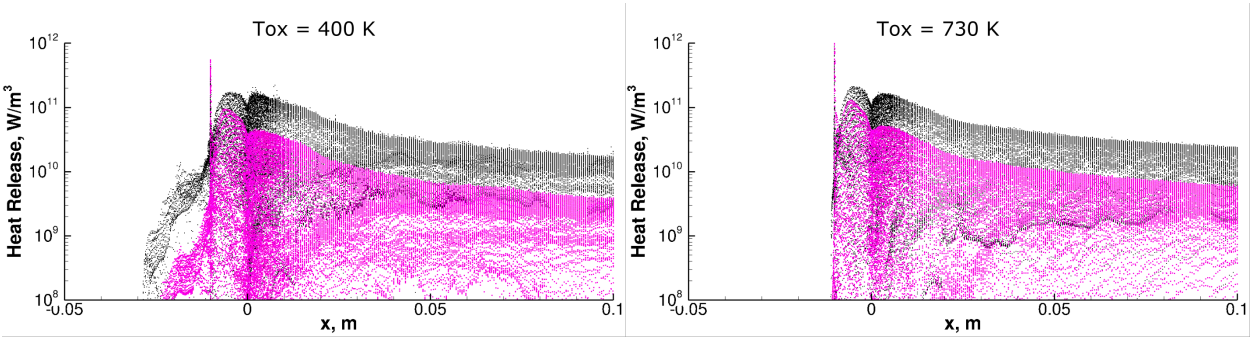

Fig. 34 Heat release statistics distribution along the length of the head-end section of the combustor. Mean heat release: color, standard deviation: black. The injector exit is located at x = 0. $T_{ox} = 400\ K$ **(L),** $T_{ox} = 730K$ **(R).**

The importance of the corner recirculation zone is also evident at the point of injector exit, where the heat release fluctuations are the strongest. The mean heat release at this location spans more than three orders of magnitude and the standard deviation surpasses the highest mean by an order of magnitude. Due to the relatively small length and time scales associated with the flames, the heat release at this condition often exhibits broad band of frequencies in the absence of a coupling with other natural modes. The instabilities generated due to a coupling, therefore appear dominant relative to the natural modes, as seen from figure 27. In order to further understand the fraction of the heat release associated with this region relative to the total heat release, consider the probability density of the heat release in the entire combustor, as shown in figure 35.

The distribution overall shows two regions, a small region centered about $10GW/m^3$ and a lower larger region at $1MW/m^3$. At the lower oxidizer temperature, the two regions are distinct, separated by a small dip in the distribution. The lower heat release region is predominantly due to relatively longer post-ignition heat release, while the highest of the heat release occurring towards the tail at the upper range, is due to ignition events. The higher oxidizer temperature shows a plateau for the high heat release region, supporting the broad band nature of the combustion at elevated oxidizer temperature. The spatio-temporal heat release variations can be better illustrated than the statistics through the reacting shear layer analysis. Compared with the prior studies with hydrogen peroxide (Smith [11], Harvazinski

[12], Sardeshmukh [5]), the current experiment uses warm gaseous oxygen as oxidizer. The altered chemical kinetics with gaseous methane as the fuel is the reason for the flame anchoring within the injector recess as seen from figure 30. This location is prone to vortex shedding, which coupled with accelerating flow of hot gases, produces a thin region of mixing before near-complete combustion. The higher temperature of the products compared to the case of hydrogen peroxide is also conducive to the recessed flame and subsequent compact flame. Such flame is visualized by isolating the mixtures within flammability limits that are at sufficient temperatures for ignition within an acoustic cycle.

The discrete locations thus identified are displayed as a function space and time in figure 36. The scatter generated is sized with equivalence ratio of the mixture and colored according to the temperature. Various instances spanning a duration longer than the cycle time of the chugging frequency are contrasted between the two oxidizer temperatures. An important aspect identified elsewhere [5] is the interaction of the reactants exiting the injector with the combustor wall. This interaction is closely related to the anchoring location as well as mixing of both reactants alone and with the hot products. The lower oxidizer temperature produces a relatively smaller acceleration of the hot gases, therefore allowing the interaction of the incoming reactants with the wall at a comparatively upstream location. The higher oxidizer temperature leads to elongated shear layer, which is nearly independent of the corner recirculation zone.

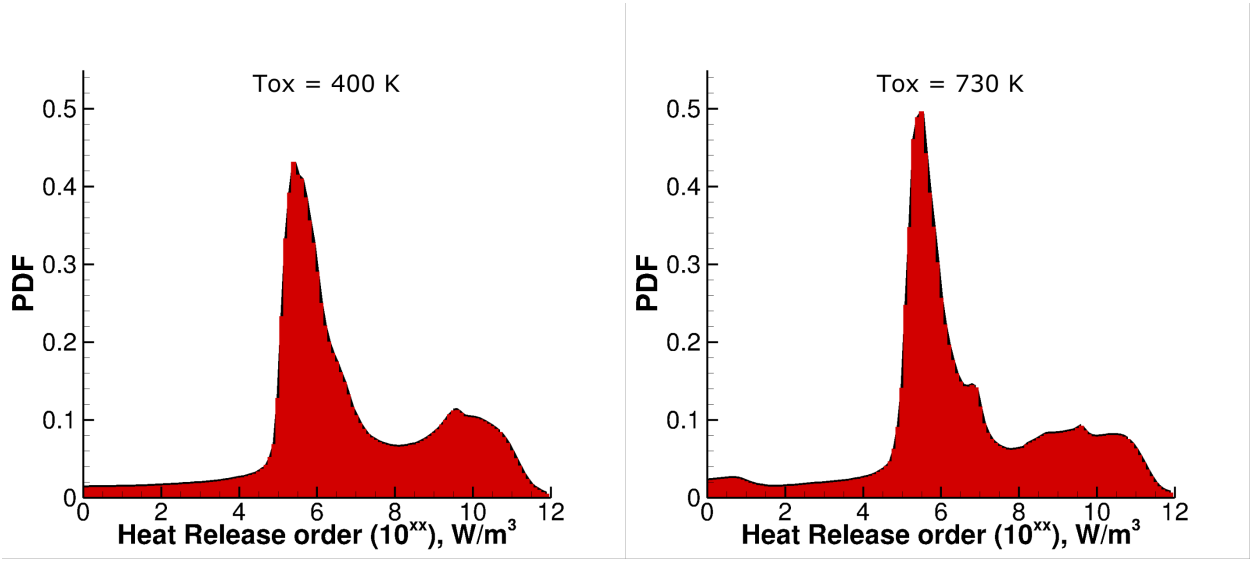

Fig. 35 Heat release probability density distribution in the combustor. $T_{ox} = 400\ K$ **(L),** $T_{ox} = 730K$ **(R).**

Heat Release and Fluid Response

An important and unique aspect of combustion dynamics in liquid rocket combustors is the very high rate of energy release. This high rate is due to high operating pressure and propellant combinations at near- stoichiometric proportions with no diluents. As a result, ignition occurs when partially premixed reactants come into contact with hot combustion products, or are locally compressed and heated by a change in pressure. At rocket conditions, very rapid ignition of these packets of reactants can result in a local pressure pulse with an amplitude approaching constant-volume combustion. This section describes an analytical and computational study of the effects of high energy release rates seen in rocket combustors. It will be shown that the amplitude of the pressure pulse, and the work done at the flow boundaries by the energy input depends on the time- and length-scales of heat addition.

Analytical Model

The pressure response of a fluid to an unsteady heat source can be analytically studied using the inhomogeneous acoustic wave equation. Equation 1 is the acoustic wave equation in one dimension with an unsteady heat source considering that the mean flow speed of sound, c_0, is spatially uniform.

$$\frac{\partial^2 p_1}{\partial t^2} - c_0^2 \frac{\partial^2 p_1}{\partial x^2} = (\gamma - 1)\frac{\partial q_1}{\partial t} \tag{1}$$

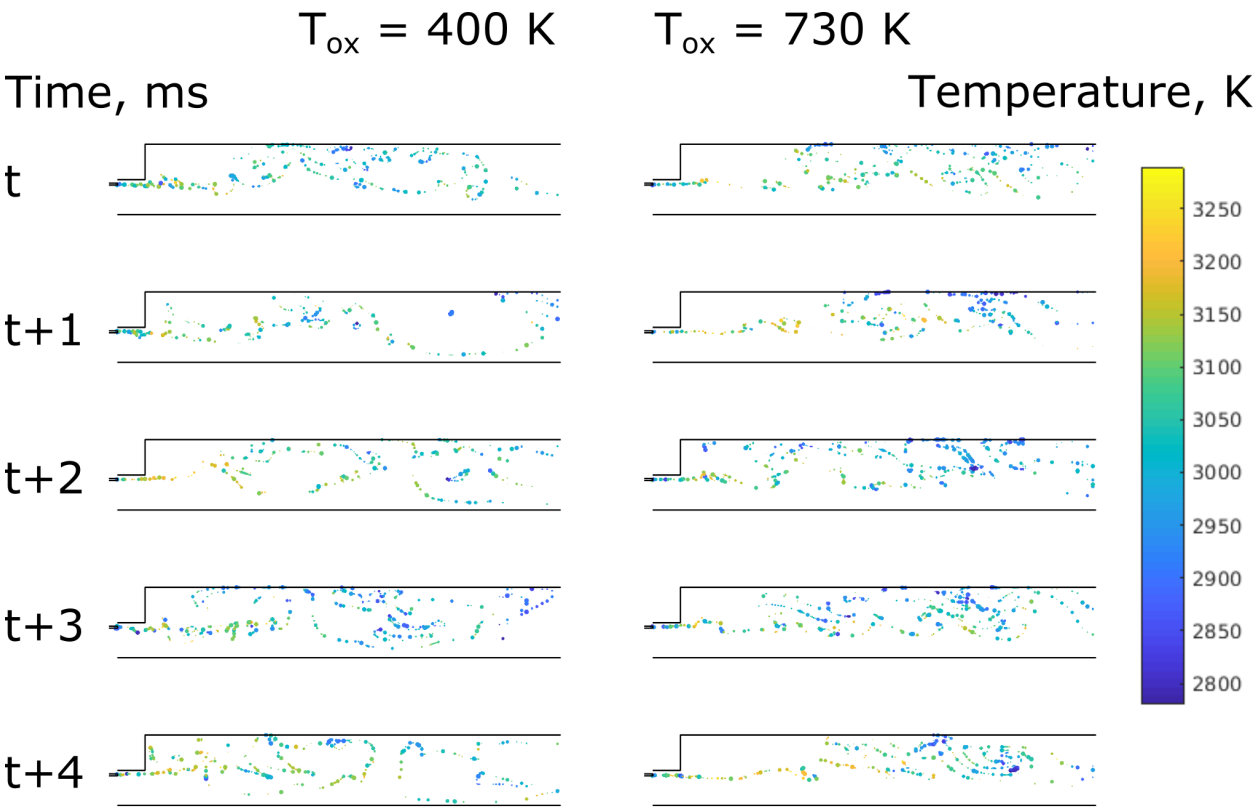

Fig. 36

An acoustic wave equation with an unsteady heat source can be derived by linearizing the equations of conservation of mass, momentum and energy (expressed in terms of entropy) by making the following assumptions and considerations (a complete derivation is presented by Dowling in [13]):

- Inviscid flow
- Thermal conduction and body forces are neglected
- Gas mixture that acts as a perfect gas, neglecting multi-species effects. The equation of state is $p = \rho RT$ and the gas constant R is given by $R = c_p - c_v$, where c_p and c_v are the specific heat capacities at constant pressure and volume, respectively.
- The flow variables are decomposed into mean flow and fluctuation parts as $\phi(\vec{x}, t) = \phi_0(\vec{x}) + \phi_1(\vec{x}, t)$.
- Small-amplitude fluctuations, keeping only linear terms ($\epsilon = \frac{\phi_1}{\phi_0} \ll 1$)
- Zero Mach number mean flow, i.e. $u_0 \simeq 0$

The analytical solution derived in this study from the acoustic wave equation with an unsteady heat source (Equation 1) assumes that the mean flow fluid properties are temporally constant and spatially uniform. The inhomogeneous acoustic wave equation problem can be posed as an initial value problem as presented in Equation 2. The initial conditions correspond to a still flow with constant $p = p_0$ across the domain. The initial conditions $\phi(x)$ and $\psi(x)$, and the source term $f(x, t)$ can be expressed as

$$\begin{cases} \dfrac{\partial^2 p_1}{\partial t^2} - c_0^2 \dfrac{\partial^2 p_1}{\partial x^2} = f(x,t) \\ p_1(x,0) = \phi(x) = 0 \\ \dfrac{\partial p_1}{\partial t}(x,0) = \psi(x) = 0 \\ f(x,t) = (\gamma - 1)\dfrac{\partial q_1}{\partial t} \end{cases} \tag{2}$$

The pressure response of the fluid is composed of the mean flow pressure and its fluctuation part, i.e. $p(x, t) = p_0 + p_1(x, t)$. In turn, the fluctuation part is composed of the homogeneous and particular solutions as $p_1(x, t) = p_{1,h}(x, t) + p_{1,p}(x, t)$.

Applying the initial conditions $\phi(x)$ and $\psi(x)$ on d'Alembert's solution, the homogeneous solution equals to zero

$$p_{1,h}\,(x,t) = \frac{1}{2}\left[\phi(x + c_0 t) + \phi(x - c_0 t)\right] + \frac{1}{2c_0}\int_{x-c_0 t}^{x+c_0 t} \psi(s)ds = 0 \tag{3}$$

The particular solution $p_{1,p}(x,t)$ can be calculated by applying the Duhamel's principle to d'Alembert's solution, which results in the following integral

$$p_{1,p}(x,t) = \frac{1}{2c_0}\int_0^t \int_{x-c_0(t-s)}^{x+c_0(t-s)} f(z,s)dzds \tag{4}$$

Since $p_{1,h}(x,t) = 0$ with these initial conditions, it follows that the pressure fluctuation $p_1(x,t)$ is only determined by the particular solution $p_{1,p}(x,t)$, which is driven by the fluctuations of the heat source term $(\gamma - 1)\frac{\partial q_1}{\partial t}$. The present case consists of a heat source per unit volume $q_1(x,t)$ with a Gaussian spatial distribution and a step temporal profile defined as

$$q_1(x,t) = \begin{cases} K_x exp\left[-\frac{1}{2}\left(\frac{x}{\sigma_x}\right)^2\right] & t_{hab} \leqslant t \leqslant t_{hae} \\ 0 & t_{hab} < t, \;\; t > t_{hae} \end{cases} \tag{5}$$

where t_{hab} is the time in which heat addition begins, t_{hae} is the time in which heat addition ends, and K_x is the heat source magnitude parameter defined as

$$K_x = \frac{E_{ha}}{\sqrt{2\pi}\sigma_x H_{ha} W_{ha}(t_{hae} - t_{hab})} = \frac{q_{ha} L_{ha}}{\sqrt{2\pi}\sigma_x} \tag{6}$$

where E_{ha} is the total energy input, and V_{ha}, L_{ha}, H_{ha}, and W_{ha} stand for the volume, length, height, and depth of the volume in which heat addition is applied, respectively. The standard deviation of the Gaussian spatial profile is set to $\sigma_x = \frac{L_{ha}}{7}$. The volumetric heat release q_{ha} corresponds to the equivalent flat profile heat release value, which integrated over space and time, inputs the same total energy input as the Gaussian profile.

$$E_{ha} = \int_{-\infty}^{\infty}\int_{-\infty}^{\infty} q_1(x,t)\; dVdt = \int_{-\infty}^{\infty}\int_{-\infty}^{\infty} q_{ha}\; dVdt = q_{ha} V_{ha} \Delta t_{ha} \tag{7}$$

where Δt_{ha} stands for the heat addition duration. Thus, the flat profile heat addition value, q_{ha}, is given by

$$q_{ha} = \frac{E_{ha}}{V_{ha}\Delta t_{ha}} = \frac{E_{ha}}{L_{ha} H_{ha} W_{ha}(t_{hae} - t_{hab})} \tag{8}$$

Hereinafter, the values of heat source intensity for the study cases are reported using the equivalent flat profile value, q_{ha}, which inputs the same heat as the Gaussian profile, as shown in Figure 37. Mathematically, the heat source function of Equation 5 is expressed as

$$q_1(x,t) = K_x exp\left[-\frac{1}{2}\left(\frac{x}{\sigma_x}\right)^2\right]\left(u(t - t_{hab}) - u(t - t_{hae})\right) \tag{9}$$

where $u(t - \tau)$ is the unit Heaviside function. Applying the temporal derivative of the heat source of Equation 9 as stated in Equation 2 yields to

$$f(x,t) = (\gamma - 1)\frac{\partial q_1}{\partial t} = (\gamma - 1)K_x exp\left[-\frac{1}{2}\left(\frac{x}{\sigma_x}\right)^2\right]\left(\delta(t - t_{hab}) - \delta(t - t_{hae})\right) \tag{10}$$

where $\delta(t - \tau)$ is the Dirac delta function. Substituting Equation 10 into Equation 4 provides the expression to be integrated to solve the pressure response

$$p_{1,p}(x,t) = \frac{1}{2c_0}\int_0^t \int_{x-c_0(t-s)}^{x+c_0(t-s)} (\gamma - 1)K_x e^{-\frac{1}{2}(\frac{z}{\sigma_x})^2}[\delta(s - t_{hab}) - \delta(s - t_{hae})]dzds \tag{11}$$

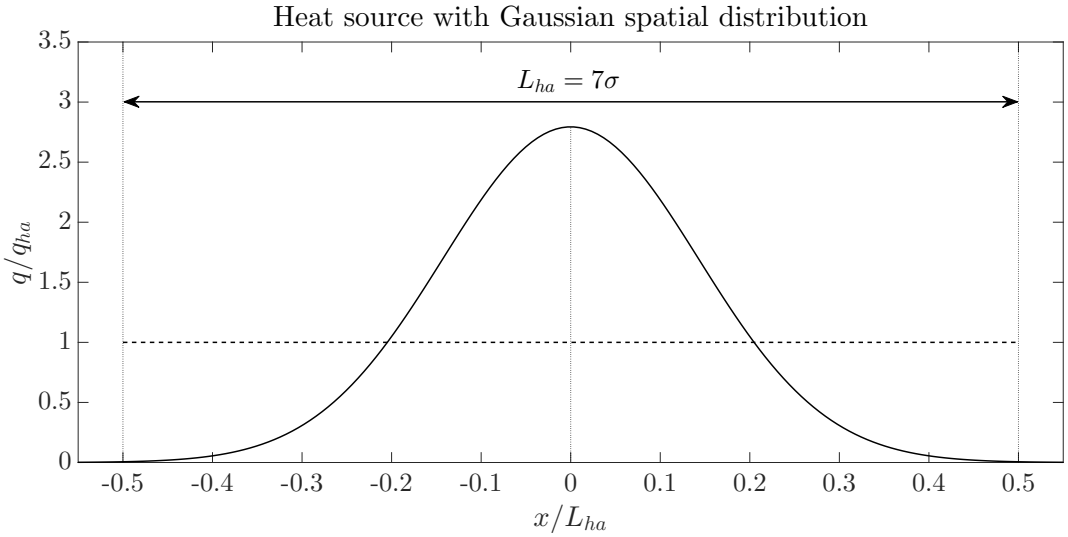

Fig. 37 Normalized Gaussian heat addition profile with respect to the flat profile heat addition intensity, q_{ha}, and the heat addition length, L_{ha}. The dashed line represents the equivalent flat profile, which has the same area under the curve as the Gaussian distribution.

Integrating Equation 11 and writing $x \pm c_0 t$ as $c_0\left(\frac{x}{c_0} \pm t\right)$, the final solution of the pressure response to an unsteady heat source with Gaussian spatial distribution and step temporal profile yields to

$$\begin{aligned} p_{1,p}(x,t) = \frac{A_{p_1}}{2}\Bigg[&\left\{erf\left(\frac{c_0}{\sqrt{2}\sigma_x}\left(\frac{x}{c_0} + (t - t_{hab})\right)\right) - erf\left(\frac{c_0}{\sqrt{2}\sigma_x}\left(\frac{x}{c_0} - (t - t_{hab})\right)\right)\right\}u(t - t_{hab}) \\ &-\left\{erf\left(\frac{c_0}{\sqrt{2}\sigma_x}\left(\frac{x}{c_0} + (t - t_{hae})\right)\right) - erf\left(\frac{c_0}{\sqrt{2}\sigma_x}\left(\frac{x}{c_0} - (t - t_{hae})\right)\right)\right\}u(t - t_{hae})\Bigg] \end{aligned} \tag{12}$$

In Equation 12 the constant multiplying all terms is precisely half the amplitude of the pressure fluctuation

$$A_{p_1} = 2\frac{(\gamma - 1)K_x\sigma_x\sqrt{2\pi}}{4c_0} = \frac{E_{ha}(\gamma - 1)}{2c_0 H_{ha} W_{ha}(t_{hae} - t_{hab})} = \frac{(\gamma - 1)q_{ha}L_{ha}}{2c_0} \tag{13}$$

Characteristic Length and Time Scales

The solution of Equation 12 contains a characteristic response time that determines the behavior of the pressure response to an unsteady heat release source with Gaussian spatial distribution and step temporal profile. From the terms inside the error functions in Equation 12, there is a constant that represents the fluid characteristic response time τ_r defined as

$$\tau_r = \frac{\sqrt{2}\sigma_x}{c_0} \tag{14}$$

For all cases studied, the standard deviation of the Gaussian heat addition profile has been set to a value of $\sigma_x = \frac{L_{ha}}{7}$. Rewriting the solution of Equation 12 in terms of the characteristic time scale τ_r yields to

$$\begin{aligned} p_{1,p}(x,t) = \frac{A_{p_1}}{2}\Bigg[&\left\{erf\left(\frac{\frac{x}{c_0} + (t - t_{hab})}{\tau_r}\right) - erf\left(\frac{\frac{x}{c_0} - (t - t_{hab})}{\tau_r}\right)\right\}u(t - t_{hab}) \\ &-\left\{erf\left(\frac{\frac{x}{c_0} + (t - t_{hae})}{\tau_r}\right) - erf\left(\frac{\frac{x}{c_0} - (t - t_{hae})}{\tau_r}\right)\right\}u(t - t_{hae})\Bigg] \end{aligned} \tag{15}$$

In turn, the velocity fluctuation can be computed from the pressure fluctuation using the linearized momentum conservation equation

$$\rho_0 \frac{\partial \vec{u_1}}{\partial t} = -\nabla p_1 \tag{16}$$

The velocity fluctuation then reads as

$$\begin{aligned} u_1(x,t) = -\frac{A_{p_1}}{2\rho_0 c_0}\Bigg[& \left\{ erf\left(\frac{\frac{x}{c_0} + (t - t_{hab})}{\tau_r}\right) + erf\left(\frac{\frac{x}{c_0} - (t - t_{hab})}{\tau_r}\right) - 2\ erf\left(\frac{x}{c_0\tau_r}\right)\right\} u(t - t_{hab}) \\ & - \left\{ erf\left(\frac{\frac{x}{c_0} + (t - t_{hae})}{\tau_r}\right) + erf\left(\frac{\frac{x}{c_0} - (t - t_{hae})}{\tau_r}\right) - 2\ erf\left(\frac{x}{c_0\tau_r}\right)\right\} u(t - t_{hae})\Bigg] \end{aligned} \tag{17}$$

The $p\nu$ work efficiency can be defined as the $p\nu$ work (also known as boundary work) generated by the pressure at the control volume boundaries divided by the total energy addition, Q. Effectively, $\eta_{p\nu}$ represents the efficiency of converting heat addition into acoustic pressure energy. The control volume is conveniently located far away of the heat addition zone in order to capture the far-field pressure response.

$$\eta_{p\nu} = \frac{W_b}{Q} = \frac{\int_0^T \oint_{\partial\Omega} p\left(\vec{u}\cdot\vec{n}\right) dsdt}{\int_0^T \int_\Omega q dV dt} = \frac{1}{Q}\int_0^T \oint_{\partial\Omega} (p_0 + p_1)\left(\vec{u_1}\cdot\vec{n}\right) dsdt \tag{18}$$

Noting that $\vec{u} = \vec{u}_1$ due to the zero Mach number assumption ($\vec{u}_0 = 0$).

There are two distinct regimes of pressure response depending on the relation between the characteristic response time τ_r and the heat addition duration Δt_{ha}:

$$\begin{cases} \Delta t_{ha} > 2\tau_r, & Full\ amplitude\ response \\ \Delta t_{ha} < 2\tau_r, & Partial\ amplitude\ response \end{cases}$$

Since the pressure response of Equation 12 is defined by the error function erf, a time of $2\tau_r$ corresponds to $erf(2)$, which implies reaching a 99.53% of the full amplitude response. Thus, $erf(2)$ has been set as the threshold to characterize the different regimes of the pressure response depending on the characteristic time scales.

1. Full amplitude response, $\Delta t_{ha} > 2\tau_r$

Under this regime, the pressure response will reach the full amplitude and propagate in both directions. Since the model neglects viscous losses, the amplitude of the pressure response does not decay over the distance.

$$p_{1_{max,FR}} = \frac{E_{ha}(\gamma - 1)}{2c_0 H_{ha} W_{ha}(t_{hae} - t_{hab})} \tag{19}$$

2. Partial amplitude response, $\Delta t_{ha} < 2\tau_r$

If the duration of heat release is short compared to the characteristic response time, the amplitude of the pressure response does not reach its full strength. The maximum amplitude occurs at $x = 0$ (center of the heat addition Gaussian profile) but decays over the distance converging to a far field value defined in Equation 21. After reaching the far field value amplitude, at a distance L_{ff} the amplitude remains constant due to the absence of loss mechanisms. The far field response occurs at a distance L_{ff} away from the center of the heat addition Gaussian profile corresponding to

$$L_{ff} = 2\tau_r c_0 = 2\sqrt{2}\sigma_x \tag{20}$$

The amplitude of the far field response is given by

$$p_{1_{max,PA}}(x > L_{ff}) = \frac{E_{ha}(\gamma - 1)}{2c_0 H_{ha} W_{ha}(t_{hae} - t_{hab})}\left[erf\left(\frac{\Delta t_{ha}}{2\tau_r}\right)\right] \tag{21}$$

It should be noted that the heat addition profiles of Figure 38 and Figure 39 input the same total energy, i.e. $Q_1 = \int_{t_{hab}}^{t_{hae}} \int_{-\infty}^{\infty} q\ dV dt = Q_2$.

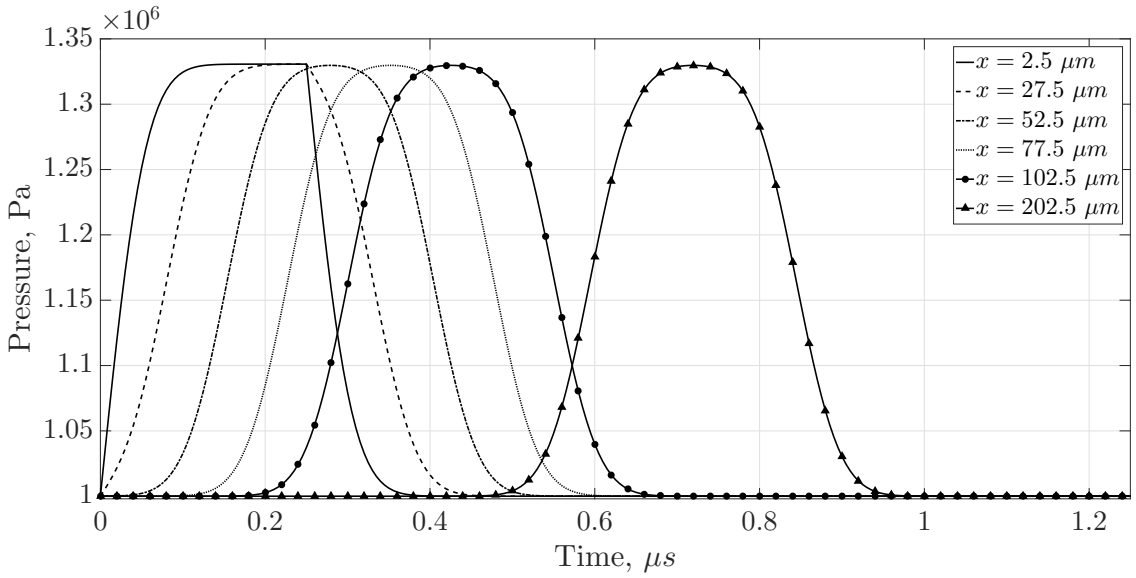

Fig. 38 Full amplitude response case. Pressure response of CO_2 at 1 MPa and 500 K to to an unsteady heat source; $q_{ha} = 1 \cdot 10^{13}\ \frac{W}{m^3}$, $L_{ha} = 100\ \mu m$ and $t_{ha} = 0.25\ \mu s$.

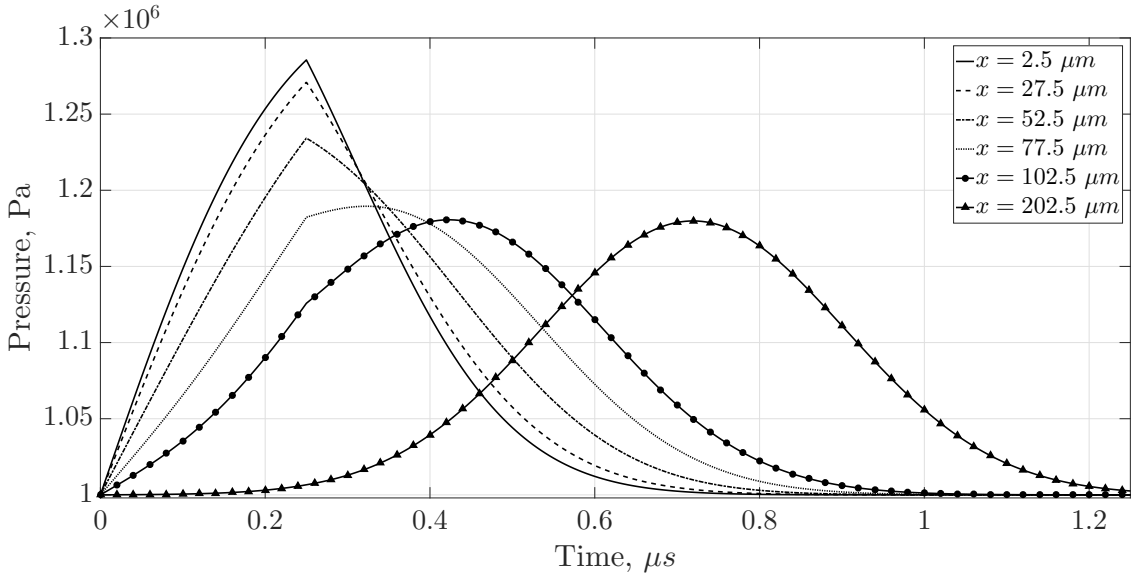

Fig. 39 Partial amplitude response case. Pressure response of CO_2 at 1 MPa and 500 K to to an unsteady heat source; $q_{ha} = 2.5 \cdot 10^{12}\ \frac{W}{m^3}$, $L_{ha} = 400\ \mu m$ and $t_{ha} = 0.25\ \mu s$. The far field distance is $L_{ff} = 161.6\ \mu m$, thus at $x = 202.5\ \mu m$ the pressure trace behaves with the far field response.

Parametric Study

This section briefly presents an analytical parametric study aimed to explore the behavior of the pressure response to unsteady heat release addition over a wide range of length and time scales. The heat addition profile used is the aforementioned Gaussian spatial distribution and step temporal profile. The parametric study has been carried out for a constant total energy input $Q = 250\ J$ (considering $H_{ha} = W_{ha} = 1\ m$). The heat addition band size L_{ha} has been varied from 10 μm to 10 cm, and the heat addition duration t_{ha} has ranged from 0.1 μs to 1 ms. CO_2 has been used as the fluid for the study, with an initial temperature and pressure of 500 K and 1 MPa, respectively. Figure 40 shows a map of the far-field fluctuation pressure amplitude of the pulses with respect to the heat addition length and duration. Both Figure 40 and Figure 41 depict the critical line $\Delta t_{ha} = 2\tau_r$ that separates the two distinct pressure response behaviors: full

amplitude response above the critical line, and partial amplitude response below it. Above the critical line, in which the heat addition duration is long with respect to the fluid characteristic response time, the amplitude of the pressure pulses is independent of the heat addition band size and only depends on the inverse of the heat addition duration. In this regime, shorter heat addition durations result in larger amplitude pressure fluctuations. Conversely, in the area below the critical line, where the heat addition duration is shorter than the characteristic response time, the fluid can only reach a partial amplitude and not reach the full potential due to its relative slow response to heat addition. In this regime, concentrating the heat addition zone in smaller band sizes results in higher amplitude of the pressure fluctuations.

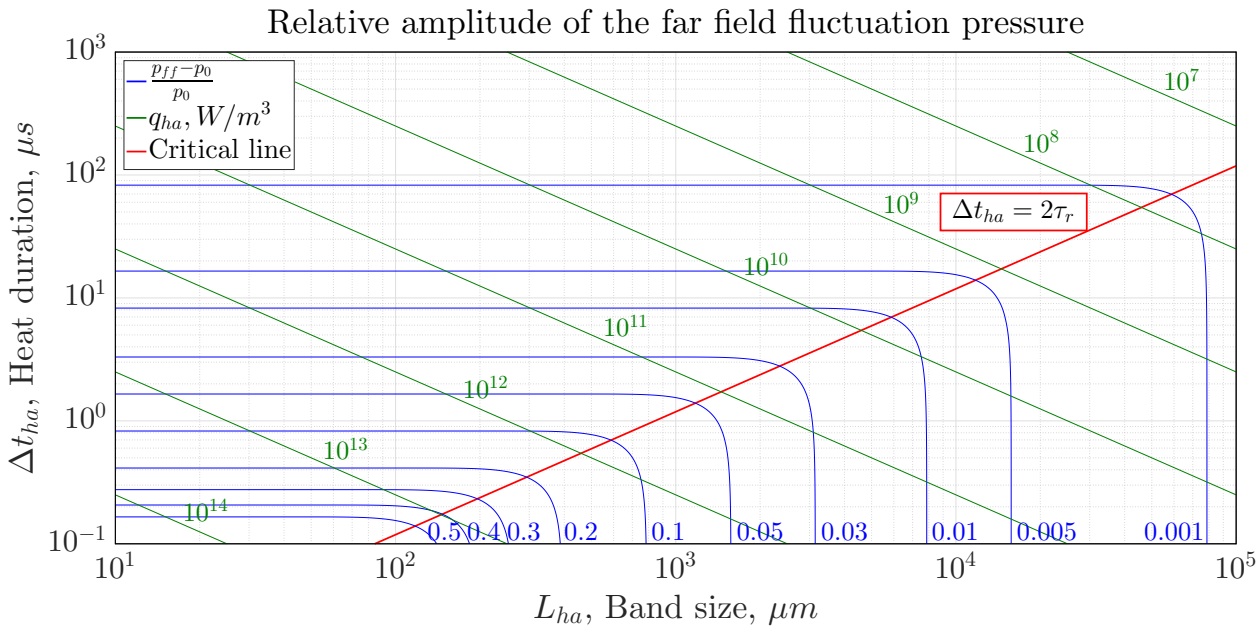

Fig. 40 Map of the far-field amplitude of the pressure response of CO_2 to different heat addition profiles. The green lines represent lines of constant heat addition rate in W/m^3, whereas the blue lines represent contours of $\frac{p_{ff}-p_0}{p_0}$.

Figure 41 shows a map of the pv work efficiency, η_{pv}, as defined in Equation 18. The pv work, also known as boundary work, W_b, represents the pressure work at the boundaries of the control volume. In this case, η_{pv} is a good metric to assess the relative amount of energy from heat addition that is converted into actual pressure work. It should be pointed out that all cases studied in this section have the exact same total energy input Q. The map of Figure 41 shows that pv work efficiency tends to increase for smaller time and length heat addition scales. The two behaviors of full and partial amplitude response are clearly distinguished by the critical line. It is important to point out that the pv work efficiency plateaus for large time and length heat addition scales. The addition of heat release in this long durations (small time rate of change of heat release) over widespread areas approaches to a regime of constant pressure combustion. On the contrary, the small time and length heat addition scales tends towards the constant volume combustion, which has higher efficiency than the constant pressure combustion regime.

Comparison of Analytical and Numerical Results

High-fidelity simulations using Purdue's in-house Navier-Stokes solver GEMS have been performed with the aim of assessing the validity of the analytical models and their limitations. Since this case is a simplified representation of an open flame, the dimensions of the domain have been set in such a way as to avoid reflected pressure waves from reaching the zone of energy addition prior to the conclusion of the simulation. The computational domain, depicted in Figure 42, consists of a two-dimensional cavity of 20 mm x 30 mm. The total number of cells is 75,072 and the mesh is divided in 96 partitions. At the zone of analysis, which comprises the heat addition events and its surroundings, the grid is uniform with a cell size of 5 μm in the x and y directions. In order to accurately capture the transient, the time step is limited to 2.5 ns and the simulations last for 12.5 μs. The study is carried out using CO_2 as it is a pure substance common in rocket combustion. A pressure of 1 MPa and a temperature of 500 K are chosen as the initial

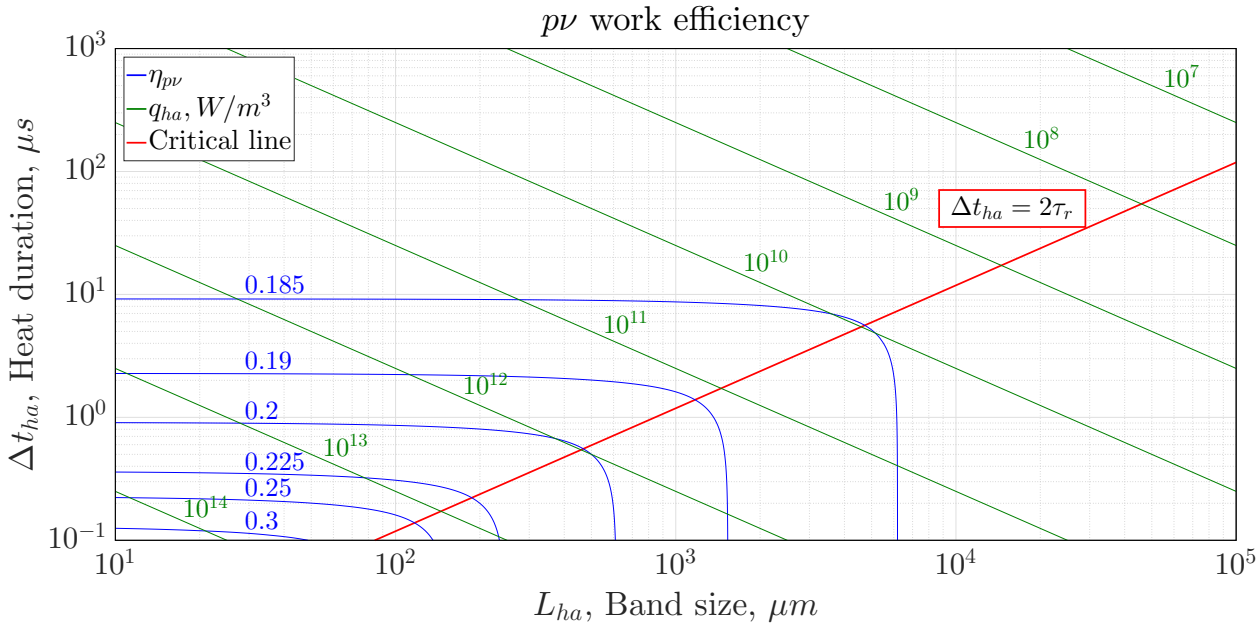

Fig. 41 Map of the $p\nu$ work efficiency of the pressure response of CO_2 to different heat addition profiles. The green lines represent lines of constant heat addition rate in W/m^3, whereas the blue lines represent contours of $\eta_{p\nu}$ (as defined in Equation 18).

conditions, which are representative of the interaction between hot and cold gases in the recirculation region of the study configuration described above. All boundaries are modeled as inviscid, adiabatic walls.

The following two plots present the comparison of the analytical solution against high-fidelity numerical simulations. The study case consists of quiescent CO_2 at 1 MPa and 500 K subjected to a heat release source with spatial Gaussian distribution and step temporal profile. The heat release flat profile value is $q_{ha} = 2.5 \cdot 10^{12}\ \frac{W}{m^3}$, which is spanned over a length $L_{ha} = 100\ \mu m$, and a time duration of $t_{ha} = 1\ \mu s$. Figure 43 shows the comparison of the numerical and analytical solutions of the pressure response to the unsteady heat release source. The analytical solution captures well the dynamics of the real case with a slight overshoot in amplitude due to the assumption of constant speed of sound and the absence of loss mechanisms (heat of conduction and viscous stresses are neglected in the analytical model).

Figure 43 and Figure 44 summarize the time evolution of the flow variables at the centerline of the Gaussian heat source and at a distance of 52.5 μm from it (since the Gaussian heat addition length is $L_{ha} = 100\ \mu m$, the latter location is right outside the heated band). Figure 43 shows that the temperature increases substantially at the center of the Gaussian heat source profile but this effect mitigates the further away it is measured from the center location. Since the speed of sound is strongly dependent on the temperature, the direct consequence of the temperature increase due to heat addition is the increase of speed of sound. However, the analytical model assumes a uniform speed of sound so that it does not capture this local effect of speed of sound increase. This difference in speed of sound is the major cause of the discrepancy between the analytical model and the high-fidelity numerical simulation.

As shown in Figure 43, by the time the pressure trace reaches the maximum value (around $t = 0.12\ \mu s$), the speed of sound has already started to increase and from there it grows quickly in a close to linear fashion. Looking at the numerical pressure solution, it is clear that this pressure relaxation after the maximum follows the same quasi-linear trend shown by the speed of sound increase or the same trend exhibited by the density. It should be pointed out that an increase in speed of sound decreases the effectiveness from which unsteady heat release generates acoustic pressure waves. The characteristic impedance, ρc, follows a very similar trend to that experienced by the density, as the latter decrease has a more dominant effect than the speed of sound increase. The comparison of Figure 43 and Figure 44 reveals that the temperature increase effects are very local and barely affect the local properties at the edge of the Gaussian heat addition band ($x = 50 \mu m$). Indeed, whereas the relation between pressure, temperature and density at the centerline are clearly nonisentropic due to the heat addition, right outside the Gaussian heat addition band the state variables essentially follow the isentropic gas relations. Therefore, in an unsteady heat release event, the shape of the pressure pulse will be completely affected by the local temperature fluctuations (which in turn vary the density, speed of

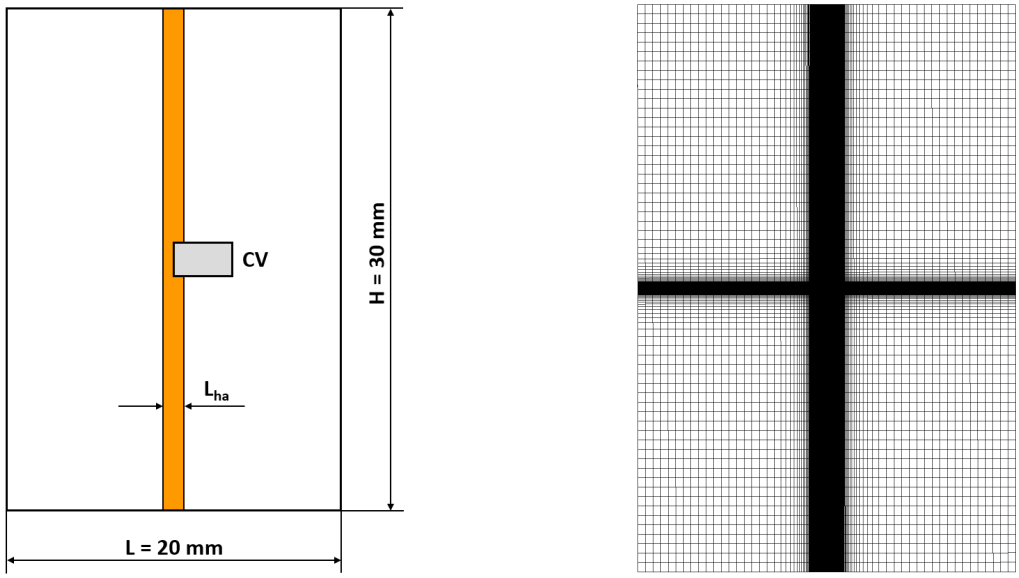

Fig. 42 Schematic of the computational domain for the heat release response simulations (L) and its computational mesh (R). The heat addition profiles are applied in the orange area.

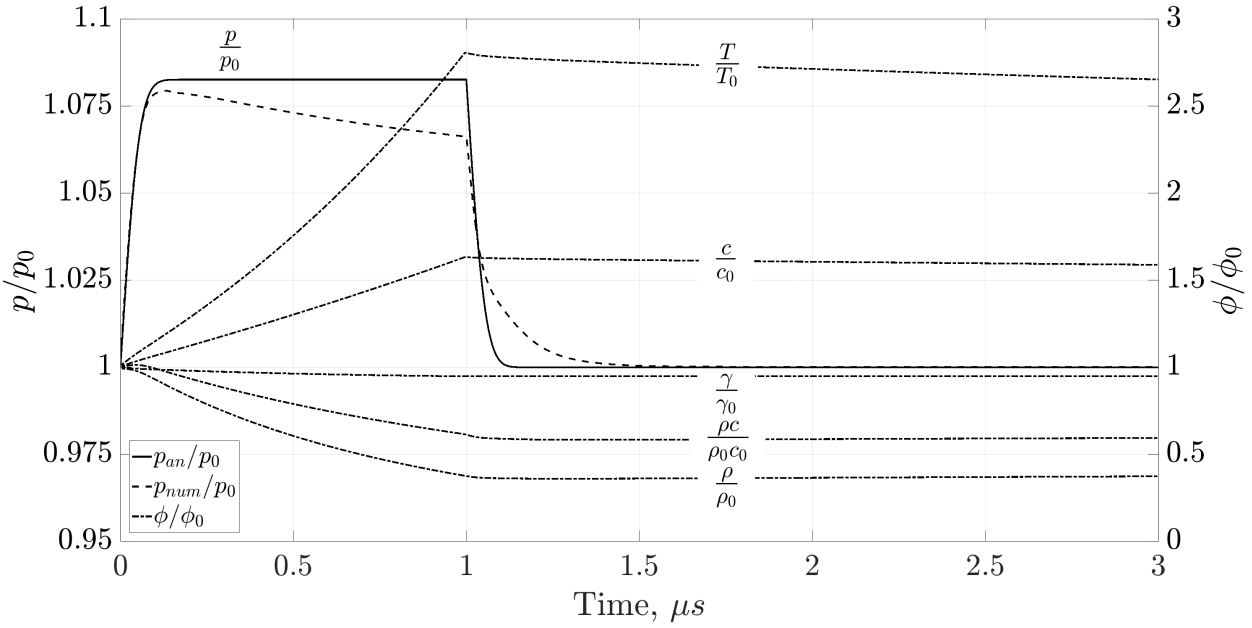

Fig. 43 Flow field response at the center line of an unsteady heat source for CO_2 at $1\ MPa$ and $500\ K$. The heat release source applies $2.5 \cdot 10^{12}\ \frac{W}{m^3}$ spanned over a length of $100\ \mu m$ and a duration of $1\ \mu s$. In the plot legend, p_{an}, p_{num}, and ϕ/ϕ_0 correspond to the pressure analytical solution, and numerical solution of pressure and the rest of flow field variables, respectively.

sound, etc.), but these will only begin to affect the surroundings much later after the pressure pulse has passed due to the slow time scale of thermal diffusion processes compared to acoustics.

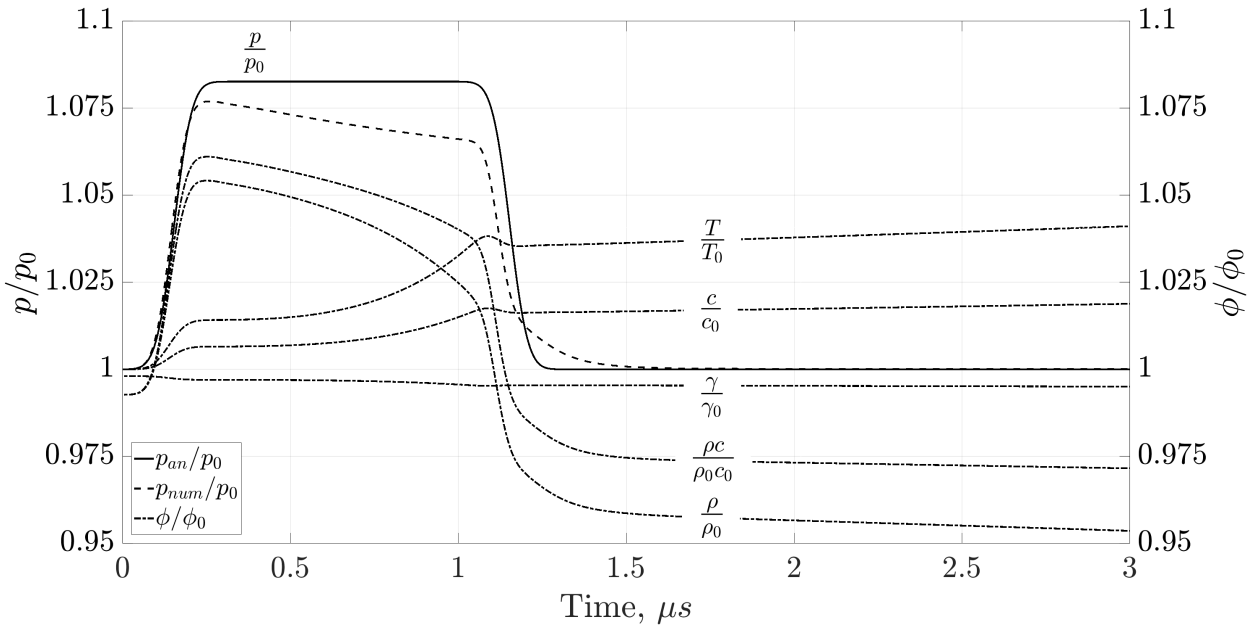

Fig. 44 Flow field response at $x = 52.5\ \mu m$ of an unsteady heat source for CO_2 at $1\ MPa$ and $500\ K$. The heat release source applies $2.5 \cdot 10^{12}\ \frac{W}{m^3}$ spanned over a length of $100\ \mu m$ and a duration of $1\ \mu s$. In the plot legend, p_{an}, p_{num}, and ϕ/ϕ_0 correspond to the pressure analytical solution, and numerical solution of pressure and the rest of flow field variables, respectively.

Summary of the Pressure Response to Unsteady Heat Release

The unsteady heat release that occurs during the ignition of a pocket of propellants in a combustor can be modeled as a heat source with a Gaussian distribution. Swaminathan proved that a Gaussian profile represents fairly well the fluctuating heat release rate and the temporal rate of change of the fluctuating heat release rate spatial correlation [14]. His analysis revealed that the planar laminar flame thermal thickness can be used as the characteristic length scale of the unsteady heat release profile. The representation of the heat release profile as a Gaussian distribution can be then linked to physical length and time scales of turbulent flames.

The study of the analytical solution has revealed two different pressure response behaviors depending on the length and time scales of the heat release profile. On the one hand, for sufficiently long heat addition durations, the amplitude of the pressure fluctuations depends only on the inverse of the heat addition duration and it is independent of the length scale of the spatial Gaussian profile. On the other hand, for durations shorter than twice the fluid characteristic response time, the amplitude of the pressure fluctuations converges to a far-field value which is lower than the potential maximum. Both phenomena have been properly captured by means of analytical and numerical results, although the analytical solutions slightly overpredict the pressure response due to the assumption of constant mean flow properties, and neglecting heat of conduction and viscous effects in the analysis. Furthermore, high-fidelity numerical simulations have revealed the existence of weak shock waves formed at a certain distance away from the heat addition zone due to wave steepening. The formation of weak shocks is a nonlinear acoustic effect caused by the variation of the local speed of sound with temperature. Based on the magnitude of heat release, which drives the amplitude of pressure fluctuations, three different regimes can be distinguished:

- Low rates of heat release (gas turbines): isentropic compressions
- High rates of heat release (liquid rocket engines): weak shocks
- Detonations (pressure-gain combustion): strong shocks

The fluid characteristic response time is directly proportional to the heat release length scale (i.e. flame thickness) and inversely proportional to the local speed of sound. The flame thickness decreases with the pressure whereas the speed of sound increases with temperature. In high-performance rocket engines the pressure and temperatures are extremely high. However, the maximum local speed of sound is bounded by the maximum temperature in the combustor, which in turn is limited by chemical reactions and has a small dependency on the chamber pressure. In contrast, the flame thickness continues to decrease with increasing pressure so that for higher operating pressures the characteristic

response time will tend to shorten. Therefore, for liquid rocket engines the realization of partial or full amplitude of pressure fluctuations due to combustion noise is mostly determined by the rate of change of unsteady heat release since the fluid characteristic response time is very short. This rate of change is inversely proportional to the unsteady heat release time scale. Liquid rocket engines suffer from a high level of unsteadiness and a succession of ignition and extinction events that result in extreme time rates of change of heat release. It is expected that for slowly varying unsteady heat release events, the pressure fluctuations will realize its full potential, and only very sharp fluctuation events might exhibit the partial amplitude response. As shown in the analytical model, the amplitude of pressure fluctuations is inversely proportional to the heat release time scale, so that faster unsteady heat release events will generate larger pressure fluctuations. In a real liquid rocket engine there is a spectrum of time scales of unsteady heat release, which will determine both the magnitude of combustion noise pressure fluctuations, and their amplitude regime (i.e. partial or full amplitude).

Presentations and Publications during Project

- Sardeshmukh, S. V., Bedard, M. J., Pons, A., and Anderson, W. E., "Investigating Heat Release Dynamics in a Self-Excited Unstable Combustor Using High Fidelity Chemiluminescence Measurements and Modeling", 2018 AIAA Aerospace Sciences Meeting, American Institute of Aeronautics and Astronautics, 2018.
- Sardeshmukh S., Bedard, M., and Anderson, W. "The Use of OH* and CH* as Heat Release Markers in Combustion Dynamics," International Journal of Spray and Combustion Dynamics, Vol. 9, issue 4, 2017, pp. 409-423.
- Pons, A., Fuller, T.L., Sardeshmukh, S., and Anderson, W. E., "Analysis of the Interactions between Acoustics and Unsteady Heat Release in a Self-Excited Single Element Combustor", 54th AIAA/SAE/ASEE Joint Propulsion Conference & Exhibit, American Institute of Aeronautics and Astronautics, 2018.
- Fuller, T.L., Gejji, R., Sardeshmukh, S., and Anderson, W. E., "Considerations Regarding the Use of Laser Ignition in High-Pressure Devices", 2019 AIAA Aerospace Sciences Meeting, American Institute of Aeronautics and Astronautics, 2019.

References

[1] Smith, G. P., Golden, D. M., Frenklach, M., Moriarity, N. M., Eiteneer, B., M. Goldenberg, C. T. Bowman, R. K. Hanson, S. Song, W. C. Gardiner Jr., V. V. Lissianski, and Z. Qin, "GRI-Mech Home Page," , 2018. URL `http://www.me.berkeley.edu/gri_mech/`.

[2] Sardeshmukh, S. V., Huang, C., Anderson, W. E., Harvazinski, M. E., and Sankaran, V., "Impact of Chemical Kinetics Mechanisms on the Predictions of Bluff Body Stabilized Flames," *54th AIAA Aerospace Sciences Meeting*, American Institute of Aeronautics and Astronautics, 2016. doi:10.2514/6.2016-1687.

[3] Wilcox, D. C., "Formulation of the $k - \omega$ Turbulence Model Revisited," *AIAA journal*, Vol. 46, No. 11, 2008, pp. 2823–2838.

[4] McBride, B. J., Gordon, S., and Reno, M. A., "Coefficients fro Calculating Thermodynamic and Transport Properties of Individual Species," Tech. Rep. NASA TM-4513, National Aeronautics and Space Administration, 1993.

[5] Sardeshmukh, S. V., Heister, S. D., and Anderson, W. E., "Prediction of Combustion Instability with Detailed Chemical Kinetics," *53rd AIAA Aerospace Sciences Meeting*, American Institute of Aeronautics and Astronautics, 2015. doi:10.2514/6.2015-1826.

[6] Bauer, A. B., "Vortex Shedding From Thin Flat Plates Parallel to the Free Stream," *Journal of the Aerospace Sciences*, Vol. 28, No. 4, 1961, pp. 340–341. doi:10.2514/8.8977.

[7] Culick, F., "Unsteady Motions in Combustion Chambers for Propulsion Systems," Tech. rep., Research and Technology Organisation of NATO, Dec. 2006.

[8] Natanzon, M. S., *Unsteady Combustion in Liquid Rocket Engines*, Mashinostroyeniye, Moscow, 1984.

[9] Knoop, E., Culick, F., and Zukoski, E. E., "Extension of the Stability of Motions in a Combustion Chamber by Nonlinear Active Control Based on Hysteresis," *Combustion Science and Technology*, Vol. 123, 1996, pp. 363–376.

[10] Isella, G., Seywert, C., Culick, F., and Zukoski, E. E., "A Further Note on Active Control of Combustion Instabilities," *Combustion Science and Technology*, Vol. 126, 1997, pp. 381–388.

[11] Smith, R., Xia, G., Anderson, W., and Merkle, C. L., "Computational studies of the effects of oxidiser injector length on combustion instability," *Combustion Theory and Modelling*, Vol. 16, No. 2, 2011, pp. 341–368. doi:10.1080/13647830.2011.631031.

[12] Harvazinski, M. E., Huang, C., Sankaran, V., Feldman, T. W., Anderson, W. E., Merkle, C. L., and Talley, D. G., "Coupling between hydrodynamics, acoustics, and heat release in a self-excited unstable combustor," *Physics of Fluids*, Vol. 27, No. 4, 2015, p. 045102. doi:10.1063/1.4916673.

[13] Dowling, A. P., and Stow, S. R., "Acoustic Analysis of Gas Turbine Combustors," *Journal of Propulsion and Power*, Vol. 19, No. 5, 2003, pp. 751–764. doi:10.2514/2.6192.

[14] Swaminathan, N., Xu, G., Dowling, A. P., and Balachandran, R., "Heat release rate correlation and combustion noise in premixed flames," *Journal of Fluid Mechanics*, Vol. 681, 2011, pp. 80–115. doi:10.1017/jfm.2011.232.